This is the peer-reviewed, final accepted version for American Mineralogist, published by the Mineralogical Society of America.
The published version is subject to change. Cite as Authors (Year) Title. American Mineralogist, in press.
DOI: https://doi.org/10.2138/am-2022-8543. http://www.minsocam.org/

Revision 1

Characterization of nano-minerals and nano-particles in supergene rare earth element mineralization related to chemical weathering of granites

Zebang Yi[a], Wei Fu[*a], Qing Zhao[a], Haotian Lu[a], Xuanni Fu[a], Peiqiang Li[a], Peng Luo[a], Zhixuan Han[a], Zhiqiang Tan[c], Cheng Xu[a,b]

[a] Guangxi Key Laboratory of Hidden Metallic Ore Deposits Exploration, Guilin University of Technology, Guilin541004, China

[b] School of Earth and Space Sciences, Peking University, Beijing 100871, China

[c]State Key Laboratory of Environmental Chemistry and Ecotoxicology, Research Center for Eco-Environmental Sciences, Chinese Academy of Sciences, Beijing 100085, China

* Corresponding author:

Name: Wei Fu

Address: College of Earth Sciences, Guilin University of Technology. Jian'gan Road No.12, Guilin 541004, China

E-mail: fuwei@glut.edu.cn

Tel. /fax: +86 0773 5897019

Abstract: Ion adsorption-type rare earth element (REE) ore deposits in South China are a major source of heavy rare earth elements (HREE) around the world which are of considerable economic and strategic significance. In these ores, REE is enriched in the clay minerals, specifically kaolinite and halloysite which are derived from their parent granitoid by the weathering process. However, the mechanisms of supergene REE mineralization remain unclear. We investigated the nature and origin of supergene REE mineralization, based on a nano-scale study of a typical REE-mineralized granite regolith profile (ΣREE_{max} = 1201 ppm) in the Dazhou

super-large ion adsorption-type REE deposit, Guangxi Province, South China. Bulk mineralogical and geochemical analysis, coupled with novel nano-characterization techniques (i.e., hollow fiber flow field-flow fractionation inductively coupled plasma–mass spectrometry [HF5-ICP-MS], scanning electron microscopy [SEM], and transmission electron microscopy [TEM]), were used to determine the nature of the nano-minerals and nano-particles in the regolith samples. X-ray diffraction and SEM-EDS analyses revealed that ion-adsorption clay minerals are dominated by platy-shaped kaolinite and rod-like halloysite (10Å and 7Å) within the regolith. The average clay mineral contents decreased from 38% to 15% from the fully weathered horizon to the semi-weathered horizon. Whereas the proportion of halloysite increased in the clay mineral fraction in the deep horizons. The REE-bearing nano-particles consist predominantly of macromolecules of organic matter (2–5 nm) and clay minerals (5–40 and 40–80 nm) according to the HF5-ICP-MS analysis. There is a close association between REE and Al contents in particles with sizes of 5–40 nm in the semi-weathered horizons and 40-80 nm in the highly weathered horizons, which indicates that nano-scale clay minerals (halloysite and kaolinite, respectively) are important REE carriers. In addition, nano-scale secondary REE mineral phases, including oxide, silicate, and phosphate, were identified by the SEM and TEM observations. These phases are typically adsorbed onto the surfaces of clay minerals, specifically rod-like halloysite, but have different occurrences in the regolith profile. Cesium-oxide (cerianite) and Ce-silicate (cerite) occur mainly in the upper horizon of the regolith profile, whereas low-crystallinity REE phosphates (rhabdophane-(La)) occur mainly in the lower horizon of the profile. Our results indicate that nano-minerals and nano-particles affect REE enrichment and fractionation during granite weathering. Migration and accumulation of REE-bearing nano-minerals were caused by leaching and neoformation of REE-bearing nano-minerals during

secondary precipitation. These processes contribute to the formation of supergene REE mineralization in granite regolith.

1. Introduction

Ion adsorption-type rare earth element (REE) deposits (also known as weathered crust, elution-deposited, or regolith-hosted REE deposits) are a critical metal resource, which are widely exploited in the renewable energy and high technology industries (Kynicky et al. 2012; Xu et al. 2017; Gulley et al. 2018; Schulz et al. 2018). Such deposits were discovered in the 1960s in Jiangxi Province, China. Investigations of this type of REE deposit are of significance for the development and exploitation of REE resources (Kynicky et al. 2012), particularly with respect to the mobilization, fractionation, and enrichment of the REEs during weathering (Compton et al. 2003). Ion adsorption-type REE deposits in granite-derived regolith have been intensively studied, which has highlighted the role of REE activation, migration, and re-enrichment of REEs from the parent granite during *in situ* supergene weathering (Wu et al. 1990; Bao and Zhao 2008; Sanematsu et al. 2013; Estrade et al. 2019; Fu et al. 2019). In such deposits, most of the REEs are thought to be adsorbed on various materials, including secondary clay minerals and Fe–Mn oxyhydroxides, in the form of exchangeable cations and hydrated complexes (Sanematsu and Watanabe 2016; Borst et al. 2020). However, this adsorption may also involve primary and secondary REE-bearing nano-particles or charged colloidal particles. In addition, some studies have reported that the REEs occur as independent nano-scale REE particles that are adsorbed onto clay minerals (Taunton et al. 2000b; Berger et al. 2014; Liu et al. 2016). This indicates that REE enrichment is closely related to the formation of secondary nano-minerals in granite regolith.

Nano-minerals are minerals with grains sizes of <100 nm (Christian et al. 2008; Hochella 2008). An increasing number of natural nano-minerals have been discovered in various geological settings, especially in different components of ore deposits (Palenik et al. 2004; Yudovskaya et al. 2006; Deditius et al. 2011; Ciobanu et al. 2012). Weathering processes are important in the formation of natural nano-minerals (Schindler et al. 2019). Previous studies have shown that weathering-derived regolith contains various nano-minerals (Chen et al. 2010; Mukai et al. 2020). These nano-minerals occur on the surfaces of weathered mineral grains or are preserved after their migration (Schindler and Hochella 2015, 2016). The morphology, structure, and occurrence of nano-minerals are variable and are affected by weathering processes (Banfield and Eggleton 1989; Ciobanu et al. 2011; Hough et al. 2011). Therefore, investigations of nano-minerals may provide unique insights into the formation of ion adsorption-type REE deposits, and guide exploration, exploitation and geometallurgy of such resources.

Rare earth element enrichment in granite-derived regolith is largely related to the adsorption of REEs on clay minerals, particularly kaolinite and halloysite (Wu et al. 1990; Sanematsu and Watanabe 2016; Yang et al. 2019; Li and Zhou 2020; Mukai et al. 2020). The concentrations of REEs in fine clay minerals (< 2 μm) are typically double those of the fully weathered horizons in regolith, the ΣREE in the fine clay minerals and the fully weathered horizons are 1682. 01 ppm and 804. 69 ppm, respectively (Zhou et al. 2018). Although kaolinite and halloysite both belong to the kaolinite group, these minerals have distinct morphologies and structures. Generally, kaolinite shows a pseudohexagonal platy morphology, whereas, halloysite displays a tubular morphology which endows it with a larger surface area compared to the platy-shaped kaolinite (Chakhmouradian and Wall 2012; Yusoff et al. 2013). Moreover, the clay mineral type, grain size, and abundance vary with depth and degree of weathering in regolith, which causes

different REE adsorption, fractionation characteristics, and subsequently causes the REE concentrations variation within granite-derived regolith. The nature of REE adsorption by clay minerals and their relationship between REE enrichment and clay mineralogy in granite-derived regolith require further study.

As such, we investigated the Dazhou REE-rich granite regolith in southeast Guangxi Province, South China, which was chosen because a super-large REE deposit has been proven by exploration works in the regolith of study area (Fig. 1 A, B). It provided an ideal case for reflecting the representative features of ion adsorption-type REEs mineralization related to chemical weathering of granites. Using a combination of nano-mineral and geochemical analytical approaches, the specific objectives of our study were to determine the distribution and occurrence of nano-scale REE phases in the granite regolith profile, and further to explore their geochemical associations with REE enrichment and fractionation. It helps to elucidate the role of nano-minerals and nano-particles in affecting supergene REEs mineralization within subtropical granite weathering terrains.

2. Geological background and regolith geology

The study area is located in the Darongshan–Shiwandashan granitic suite, which is in southwestern South China (Fig. 1). The suite is located in the NE–SW-trending Hercynian–Indosinian fold belt in Qinzhou. This suite extends from near Wuzhou in the north to Dongxing in the southwest, and is controlled by the Cenxi–Bobai and Lingshan–Tengxian faults and their secondary faults. Hercynian (mainly Permian) to Indosinian (mainly Triassic) intrusive and volcanic rocks are widely exposed in the granitic belt over an area of >10,000 km^2 (Jiao et al. 2015). From northeast to southwest, the belt can be divided into five main units: Darongshan

120 batholith, Pubei batholith, Jiuzhou pluton, Taima pluton and Nadong pluton (Chen et al. 2011).
121 The exposed strata are of Cambrian–Cretaceous, Paleogene, and Neogene age (Chen et al. 2011;
122 Fu et al. 2019).

123 The Dazhou granite is located at the northwestern margin of the Darongshan granite in the
124 Darongshan–Shiwandashan granite belt in Pingnan county, Guangxi Province, and is one of the
125 few Hercynian K-feldspar granites in South China (Wang 1991). The Dazhou granite is ~64 km
126 in length and 2-8 km in width, and exposed over an area of 238 km^2 (Li 2014). The granite body
127 is elongated in a NE–SW direction, parallel to the Lingshan–Tengxian fault zone. The Dazhou
128 granite was intruded into Cambrian, Ordovician, and Devonian metamorphic and sedimentary
129 rocks, which were partially buried by Lower Jurassic and Cretaceous strata. The Dazhou granite
130 is a single-stage batholith consisting mainly of medium- to coarse-grained biotite hornblende
131 moyite and medium-grained biotite hornblende adamellite granite. The Dazhou granite is
132 gradationally zoned from medium- to coarse-grained biotite hornblende moyite (with some
133 feldspar phenocrysts) in its core to fine- to medium-grained biotite hornblende moyite at its
134 margin. Fine-grained biotite hornblende moyite occurs locally at the margins of the batholith.
135 The main minerals in the granite are K-feldspar, plagioclase, quartz, and biotite, along with a
136 minor amphibole and accessory apatite, monazite, zircon, magnetite, ilmenite, and allanite (Li
137 2020). The Dazhou granite is an S-type granite with an age of *ca*. 283 Ma (Min et al. 1995).

138 The study area has a subtropical monsoonal climate, and is characterized by hot and humid
139 weather (annual average temperature ~21.7°C), abundant rainfall (annual rainfall ~1650 mm),
140 and well-developed vegetation. Under these conditions, chemical weathering of the granite is
141 intense, and the batholith is strongly weathered and characterized by moderately undulating low
142 mountains and hills with elevation varying from ~40 to 350 m above sea level. Regolith is

widely developed and well-preserved, with a thickness of 5–30 m, although locally it can be >50 m thick. The samples were collected from a profile located at 23°18′45.40″N and 110°33′11.09″E (Fig. 1). The profile is clearly zoned and can be divided from top to bottom into a topsoil layer, and fully weathered (FWH), highly weathered (HWH), and semi-weathered (SWH) horizons, based on color, structure, and mineralogy (Fig. 2). The topsoil layer is also known as the residual slope layer, and is mostly brown in color and contains quartz and clay minerals. The FWH is mostly red to reddish brown in color and comprises soft soil in which clay minerals are the predominant mineral phases. The HWH is yellow–brown in color, and has a loose structure and high content of clay minerals and low content of quartz. The FWH and HWH are the main REE-rich layers. The SWH is yellow–brown to yellow–white in color, contains residual fragments of the parent rock, and has a sandy texture. The SWH consists of clay minerals and a small amount of silicate rock-forming minerals (Fig. 2).

3. Sampling and analytical methods

Eleven samples (LC-01 to -11) were collected from the various layers in a typical regolith profile of the Dazhou granite (Fig. 2). The regolith samples of ~500 g were collected at sampling intervals of 0.5 m using a hand shovel and were stored in polyethylene bags. Three samples from the FWH, four samples from the HWH, four samples from the SWH and a bedrock sample were collected within regolith profile. After sampling, the collected samples were sieved through a 2 mm sieve to remove gravel and large organic material. The sieved material was air-dried at room temperature. In this study, samples from three horizons (FWH, HWH, and SWH) were selected for analysis.

3.1 Sample digestion and ICP–MS analysis

For the analysis of REE, approximately 50 mg of sample powder was weighed and placed in a Teflon bomb. A mixture of 1 mL of distilled HNO_3 and 1 mL of HF was slowly added to the Teflon bomb. The bomb was then sealed and placed in a stainless steel pressure jacket and heated to 190℃ in an oven for >24 h. After cooling, the Teflon bomb was opened, placed on a hotplate at 140℃ and evaporated to incipient dryness, and then 1 mL of HNO_3 was added and evaporated to dryness again. Once dry, 1 mL of HNO_3, 1 mL of MQ water, and 1 mL of 1 ppm In were added to the bomb, which was then resealed and placed in an oven at 190℃ for >12 h. The final solution was transferred to a polyethylene bottle and diluted to 100 g with 2% HNO_3. The reagent blanks were subjected to the same procedures as the samples.

Elemental concentrations of the digested samples were determined with an Agilent 7900 inductively coupled plasma–mass spectrometer (ICP–MS). The analytes chosen were Sc, Y, La, Ce, Pr, Nd, Sm, Eu, Gd, Tb, Dy, Ho, Er, Tm, Yb, Lu. Instrumental precision was constrained by analysis of laboratory standard solutions at the beginning and the end of the ICP-MS analysis. Uncertainties of the REE analyses are less than ±6% (1σ). The ICP–MS analyses were conducted at the Guangxi Key Laboratory of Hidden Metallic Ore Deposits Exploration, Guilin University of Technology, Guilin, Guangxi Province, China.

3.2 X-ray diffraction analysis

3.2.1 Bulk mineralogy

The X-ray diffraction (XRD) data were obtained with a Philips X'Pert MPD diffractometer, which uses a Cu target and is operated at 40 kV and 100 mA. The XRD analyses were undertaken at the Guangxi Key Laboratory of Optical and Electronic Materials and Devices,

Guilin University of Technology. The scanning rate was 2° min^{-1} over a 2θ range of 5°–90°. For routine XRD phase identification, a particle size of less than 20 μm is required, which is achieved by standard grinding and mounting in an agate mortar and pestle. Qualitative analysis was first conducted to determine the mineralogy of the samples with Highscore software (Degen et al. 2014). The Rietveld method was then used to obtain quantitative mineral data, which was conducted with TOPAS software (Academic version 5.1) in combination with coding program jEdit (Coelho 2018; jEdit 2022). The basis of the quantitative analysis is the full spectrum fitting refinement (Hill and Howard 1987). This comprises a numerical simulation of the XRD pattern using the least squares method based on both the instrumental conditions used for data collection and crystallographic information of the phases identified in the samples (Rietveld 2014). Background determination followed an algorithm by Sonneveld and Visser (1975). During Rietveld refinements, the scale factor, which is related to the weight fraction of the phases, was allowed to vary along with all other parameters. Following Andrade et al. (2018), the first refinement step was to correct for sample displacement with respect to the focal circle of the instrument. The next step was to adjust the cell parameters for all the minerals phases, based on their crystallographic information files, which is an independent fit to the peak positions, shapes and intensities. The results are then corrected to maximize the agreement between the calculated and experimental peak broadening which was made for phases > 5 wt.% to obtain more accurate quantitative mineral data.

3.2.2 Clay mineralogy

After removing organic materials and carbonate using 10% hydrogen peroxide (H_2O_2) and 0.1 N hydrochloric acid (HCl), respectively, the regolith samples were separated for clay mineral

(<2 μm) differentiation according to Stokes' settling velocity principle by sedimentation. We used the sedimentation method by placing the sample in a beaker with an inner diameter of 7 cm and a height of 10 cm at an experimental temperature of 19˚C. The sedimentation time was calculated as 4 hours and 10 minutes according to the Stokes formula, and the upper 5 cm of liquid was extracted, followed by centrifugation at 5000 rpm for 10 minutes, and the smear was made into a natural slice; the natural slice was heated in an oven at 60 ˚C for 24 hours to make ethylene glycol saturated slides for the subsequent test. Subsequently, the oriented glass with clay minerals was measured by standard X-ray diffraction (XRD) using a D8 ADVANCE diffractometer with CuKa radiation at the Key Laboratory of Marine Geology and Environment, Institute of Oceanology, CAS. The clay mineralogy determination was based primarily on the position of the (001) series of basal reflections on the XRD diagram of the ethylene-glycol salvation.

3.3 Hollow fiber flow field-flow fractionation inductively coupled plasma–mass spectrometry analysis

3.3.1 Nano-particle extraction

Nano-particles from the HWH and SWH (LC-04 and LC-09) samples were extracted using the aqueous method of Regelink et al. (2013) and Yi et al. (2020) for hollow fiber flow field-flow fractionation ICP–MS (HF5–ICP–MS) analysis. The nano-particle extraction consisted of four steps, as follows. (1) A 2 g regolith sample was mixed with 40 mL of sodium pyrophosphate ($Na_4P_2O_7$; TSPP) solution in a 50 mL centrifuge tube and placed on a shaker at 200 rpm for 24 h, to promote ion exchange and remove the nano-particles from the sample matrix.

(2) The suspensions were then ultrasonicated for 0.5 h to disaggregate microaggregates and

235 release the nano-particles.

236 (3) The suspension was then centrifuged to obtain the desired nano-particles with sizes of <100
237 nm according to the following equation:

$$t = \frac{\eta \lg(R_1/R_2)}{3.81N^2r^2\Delta d^2}.$$

238 This equation calculates the time (t) required for centrifugation. R_1 is the distance from the liquid
239 level in the centrifugal tube to the center of the rotor axis (in cm), R_2 is the distance from the
240 suspended particles to the center of the rotor axis (in cm), N is the centrifugation speed (in
241 revolutions s^{-1}), r is the particle radius in the suspension, Δd is the density difference between the
242 nano-particles and aqueous solution (assumed to be 1.65 g cm^{-3}), and η is the viscosity of the
243 medium (0.01005 g cm^{-1} s^{-1} at 20°C).

244 (4) The extracted nano-particles were removed from the centrifuge tubes and transferred to
245 acid-washed centrifuge tubes and stored in the dark at 4℃ until further analysis. The nano-
246 particle extraction procedure was performed at the Guangxi Key Laboratory of Hidden Metallic
247 Ore Deposits Exploration, Guilin University of Technology, Guilin, Guangxi Province, China.

248

249 **3.3.2 HF5–ICP–MS setup**

250 The sample separation and fractionation methods of the hollow fiber flow field-flow
251 fractionation (HF5) system have been described elsewhere (Tan et al. 2015). In brief, nano-
252 particle separation and fractionation were conducted in a cylindrical hollow fiber (HF)
253 membrane instead of the thin, ribbon-like, open channel in the HF5 system, and the flow field
254 was applied perpendicular to the HF axial direction. The samples were separated and fractionated
255 based on their different hydrodynamic diameters, which results in a different elution time within
256 the channel. The sample fractions eluted during the fractionation process were then analyzed by

an ICP–MS coupled to the HF5 system. The entire analytical run cycle consists of three on-line steps: (1) focusing/relaxation of the nano-particle suspension and isolation of the nano-particles; (2) separation, fractionation, and characterization of the nano-particles in the channel of the HF5 system; and (3) identification and quantification of the nano-particles by coupling to the ICP–MS.

The HF5 carrier solution consisted of 0.02% (w/v) NaN_3 (Biograde; Fisherbrand) and 0.1% (v/v) FL-70 (Fisherbrand) in deionized water (>18 MΩ cm^{-1}). The detector flow was set to 1.0 mL min^{-1}, and a cross flow of 1.2 mL min^{-1} was applied for 24 min. The sample injection volume was 100 μL, with a 6 min focus time. Standard polystyrene nanospheres (PS NPs) with diameters of 20, 40, and 80 nm (NIST; Gaithersburg, USA) were used to calibrate the particle size with respect to elution time. An ultraviolet–visible spectrometer (Agilent 1200 VWD) was used to record the elution times of the PS NPs for the calibration. The ultraviolet–visible spectrometer and ICP–MS parameters are presented in Table 1. The ICP–MS analyses were carried out at the State Key Laboratory of Environmental Chemistry and Ecotoxicology, Research Center for Eco-Environmental Sciences, Chinese Academy of Sciences, Beijing, China.

3.4 Scanning electron microscopy

The micro- to nano-scale morphology of clay and REE minerals in the regolith samples were observed with a ΣIGMA 300 field emission scanning electron microscope (FE-SEM). The SEM imaging and analyses were conducted in the Guangxi Key Laboratory of Hidden Metallic Ore Deposits Exploration, Guilin University of Technology. The particles were examined by back-scattered electron (BSE) and secondary electron (SEI and In-lens) microscopy, and quantitative chemical analyses were obtained by energy dispersive X-ray spectrometry (EDS).

This is the peer-reviewed, final accepted version for American Mineralogist, published by the Mineralogical Society of America.
The published version is subject to change. Cite as Authors (Year) Title. American Mineralogist, in press.
DOI: https://doi.org/10.2138/am-2022-8543. http://www.minsocam.org/

The optimal resolution of the SEM is 1.3 nm. The SEM was operated at an accelerating voltage of 0.1–30 kV, with a beam current of 4 pA to 20 nA. The analytical errors of the elemental concentrations are approximately ±3%.

3.5 Transmission electron microscopy

Nano-particles in the regolith samples were examined with a JEM-2100F transmission electron microscope (TEM) (point resolution = 0.25 nm; line resolution = 0.104 nm, LaB_6 source; maximum accelerating voltage of 200 kV) equipped with an energy dispersive X-ray spectrometer. The TEM analyses were undertaken at the Guangxi Key Laboratory of Optical and Electronic Materials and Devices, Guilin University of Technology. TEM samples were prepared using the drop deposition method as described in previous studies (Baalousha et al. 2014; Prasad et al. 2015). TEM grids were functionalized using positively charged Poly-L-Lysine (1% w/v in a water solution; Ted Pella, USA) to enhance the attachment of negatively charged nano-particles to the grid surface. Crystallographic information was obtained from selected area electron diffraction (SAED) analysis. Analysis of the diffraction patterns was undertaken with Digital Micrograph™ 3.11.1 software.

4. Results

4.1 Whole-rock rare earth element geochemistry of the granite regolith

The variations in the pH, total REE (ΣREE), light REE (LREE), heavy REE (HREE), and δCe values in the regolith profile of the Dazhou granite are shown in Figure 3. The ΣREE and LREE values exhibit different trends, whereas, the HREE shows different trend compared to the ΣREE and LREE values. The ΣREE and LREE values increased slightly within the FWH (LC-1-

LC-3), increased sharply from the FWH to the HWH (LC-3- LC-7) and the upper SWH (LC-8- LC-9), and diminished sharply in the bottom SWH (LC-10- LC-11), which show an "arch back" distribution pattern along the vertical profile according to their concentration variation in different horizons. The HREE values increased slightly within the FWH and HWH (LC-1- LC-7), increased sharply within the SWH (LC-8- LC-9), and diminished sharply from the upper SWH to the bottom SWH. In general, ΣREE contents vary from 176 to 1201 ppm, with an average value of 638 ppm within the profile. From the chondrite-normalized REE profile (Fig. 4a), the LREE-rich patterns (LREE/HREE > 3) with a negative Eu anomalies of the soil horizons fundamentally inherit from the parent rock. With increasing depth, Ce anomalies change from positive in the FWH (LC-1- LC-3) to negative in the HWH (LC-4- LC-6) and upper SWH (LC-7- LC-9). In the middle and lower parts of the profile (LC-4- LC-9), ΣREE contents vary from 848 to 1201 ppm (Fig. 3), and the REEs are strongly enriched (Fig. 4b).

Measured pH values of the Dazhou regolith samples vary from 5.02 to 6.03 (Fig. 3). The pH values increase from the FWH to SWH, and the lowest and highest pH values were measured at the top and bottom of the profile, respectively. The mean pH values of FWH, HWH and SWH are 5.07, 5.35, and 5.79. These pH values indicate changes in the chemical conditions in different horizons of the profile: in South China, the atmospheric precipitation is weakly acidic (Sun et al. 2010; Huo et al. 2011), and the topsoil contains more humid acid (Fu et al. 2019); when leaching downward, weathering process continues consume the H^+ from the precipitate fluids causing the pH rises within the regolith (Li et al. 2017).

4.2 Modal proportion of bulk minerals from XRD patterns

Bulk mineral compositions compositions were identified in the regolith horizons based on

the XRD patterns, and their relative proportions were determined (Fig. 5). Figure 5 shows the representative XRD results for the FWH (samples LC-1 and -2), HWH (samples LC-4 and -5), and SWH (samples LC-9 and -10) in the granite regolith profile. With progressive weathering, the proportion of quartz gradually increases to 40% on average in the SWH, 42% on average in the HWH, and 55% on average in the FWH. The proportion of orthoclase gradually decreases from an average of 42% in the SWH to an average of 35% in the lower HWH (LC-6 and LC-7), and diminished in the upper HWH and FWH. The abundance of kaolinite group minerals is 15% on average in the SWH, 32% on average in the HWH, and 38% on average in the FWH. Goethite and hematite occurs as a trace mineral with average amount < 2% throughout the soil profile. Generally, goethite occurs in the SWH and lower HWH contains, whereas with progressive weathering, hematite appears in the upper HWH and FWH.

4.3 Clay mineralogy

The clay fraction (< 2μm) in the Dazhou granite regolith are mainly kaolinite and halloysite (a mixture of 7 Å and 10 Å specie) according to their highest peak intensities at ~7.2 Å and 10.0 Å (Fig. 6). Other minerals includes montmorillonite, muscovite/illite appear in a relatively low abundance, with relatively low peak intensities. It can be seem in Figure 6, peak height of ~8.7° (10 Å) continues to increase from FWH to SWH, whereas the peak height of ~12.3° (7.2 Å) continues to decrease from FWH to SWH. This indicates that the abundance of halloysite gradually decreases with progressive weathering in the regolith profile, whereas the abundance of kaolinite increases from the SWH to the FWH. The < 2μm fraction of the SWH (LC-9) and HWH (LC-6) samples (showing the highest and lowest ΣREE contents within the SWH and HWH, respectively) were further selected to measure the SSA using the BET method (S_{BET}). The

This is the peer-reviewed, final accepted version for American Mineralogist, published by the Mineralogical Society of America.
The published version is subject to change. Cite as Authors (Year) Title. American Mineralogist, in press.
DOI: https://doi.org/10.2138/am-2022-8543. http://www.minsocam.org/

349 S_{BET} of these two samples were 14.5 m^2/g and 4.6 m^2/g, respectively. This suggests that with the
350 increasement of the proportion of halloysite, it significantly increase the overall SSA of the clay
351 fraction in the regolith profile.

352 SEM images show that the kaolinite in the regolith samples has a sheet- and plate-like habit
353 (i.e., an irregular hexagonal shape) (Fig. 7 A, B), whereas the halloysite typically exhibits a
354 euhedral and tubular or acicular habit (Fig. 7 C- F). The edges of some platy kaolinite crystals
355 are curved, and nano-tubular halloysite is developed on platy kaolinite (Fig. 7 C- F). There are
356 differences in the species of clay minerals in the HWH and SWH. The clay minerals in the HWH
357 are mainly platy kaolinite, whereas those in the SWH are mainly platy kaolinite and rod-shaped
358 or hollow–tubular halloysite (Fig. 7). The SEM observation is consistent with the XRD results.

359 **4.4 Nano-scale clay and rare earth element geochemistry**

360 Samples of the HWH (LC-4) and SWH (LC-9) were selected for HF5–ICP–MS analysis.
361 Based on the HF5–ICP–MS data, REEs (Ce, La, Nd, and Y) are predominantly present as nano-
362 particles with their peak ranges of 2–5, 5–20, and 20–80 nm (Fig. 8). The first REE peak with a
363 hydrodynamic diameter of 2–5 nm is characterized by strong UV_{254} absorbance. This can be
364 attributed to the elution of organic-rich or -bound REE nano-colloids (Siripinyanond et al., 2002;
365 Regelink et al., 2013; Stolpe et al., 2013). REE fractionation is evident between these two
366 different samples (HWH and SWH) which presents as REE peaks associated with different Al
367 peaks for the 5–80 nm size range. In the SWH sample, the Al peak occurs mainly in the particle
368 size ranges of 5–40 and 40–80 nm, which may represent two different clay minerals with
369 different morphologies and sizes (i.e., the rod-like halloysite smaller in size and platy kaolinite
370 larger in size). The main REE peak is mainly associated with the particle size range of 5–40 nm,
371 indicating that the REEs are mainly associated with halloysite. In the HWH sample, Al is only

372 associated with the particle size range of 40–80 nm, which may suggest that the clay minerals in
373 this layer are mainly platy kaolinite with a larger hydrodynamic diameter. The REE peak in the
374 HWH is mainly associated with the particle size range of 20–80 nm, and largely coincides with
375 the Al peak. This may indicate that some REEs have been desorbed from the kaolinite. The HF5–
376 ICP–MS results for the SWH and HWH reveal a significant loss of fine clay particles (5–40 nm)
377 in the upper horizons (HWH) and relative enrichment of fine particles in the lower horizons
378 (SWH) that are REE-bearing (Fig. 8).
379

380 **4.5 Rare earth element mineralogy**

381 FE–SEM and TEM–EDS were used to examine the occurrence of the REE particles.
382 Compared with the clay minerals, the REE-bearing nano-particles are brighter in BSE images.
383 However, the SEM images provide better constraints on the morphology of the nano-minerals.
384 Therefore, these two methods were both used in this study.

385 **4.5.1 Scanning electron microscopy observations**

386 In the SEM and BSE images, several bright spots of nano-scale (<100 nm) to nearly
387 micron-size (1 μm) were identified at the surfaces or edges of the clay minerals in the regolith
388 samples. The EDS analysis revealed that these bright particles consist mainly of LREEs, in
389 particular, La, Ce, Nd, and less HREE, in particular, Y. Based on the elemental composition of
390 the REE particles, they can be divided into two sub-groups: individual Ce oxide particles, and
391 La, Nd, and Y phosphate particles. SEM imaging showed that the REE particle-bearing clay
392 minerals are different in the various regolith horizons. In the HWH, the REE particles are mainly
393 adsorbed onto platy kaolinite, whereas in the SWH, the REE particles are mainly adsorbed onto
394 needle- or rod-like halloysite (Fig. 9). These nano-scale observations are consistent with the

This is the peer-reviewed, final accepted version for American Mineralogist, published by the Mineralogical Society of America.
The published version is subject to change. Cite as Authors (Year) Title. American Mineralogist, in press.
DOI: https://doi.org/10.2138/am-2022-8543. http://www.minsocam.org/

395 HF5–ICP–MS results that Ce and La, Nd, Y are separately associated with Al in different size
396 range (Fig. 9). Although SEM imaging can provide information about the particle size and REE
397 composition, it cannot further characterize the nano-structure of the REE particles. Thus, further
398 investigations were conducted by TEM.
399
400 **4.5.2 Transmitted electron microscopy observations**
401 TEM was used to analyze the suspensions extracted from the regolith samples. Figure 10
402 shows the TEM data and EDS composition of a nano-mineral. Figure 10a shows a TEM image of
403 a Ce-rich nano-particle with a size of ~100 nm, along with EDS data for the mineral after
404 removing the composition of the TEM grid. The nano-particle contains mainly Ce, Si and O, and
405 a small amount of Fe, Na, Mg and Ca, indicating it is a REE silicate. Figure 10b also shows the
406 selective area electron diffraction (SAED) pattern of the nano-particle. The SAED pattern
407 exhibits polycrystalline rings, with corresponding d-values of 1.63, 1.91, 2.69, and 3.12 Å,
408 respectively. These measured d-values are consistent with the (311), (220), (200), and (111)
409 planes of cerite and, as such, this REE-bearing nano-particle can be identified as a nano-cerite
410 $(Ce, Ca)_9(Mg, Fe^{3+})(SiO_4)_3(SiO_3OH)_4(OH)_3$.
411 Figure 10c shows another TEM image of a Ce-rich nano-particle with a size of ~100 nm.
412 The nano-particle contains mainly Ce and O, indicating it is a REE oxide. According to the FFT
413 pattern created from the HRTEM image (Figure 10e), this particle was identified as a nano-
414 cerianite (CeO_2).
415 REE-bearing particles containing La, Nd and Y with P and O were also frequently observed
416 among the SWH samples. These nano-particles show a poor crystallinity, SEAD pattern is
417 unable to acquire during the TEM observation. Several sets of lattices were occasionally

This is the peer-reviewed, final accepted version for American Mineralogist, published by the Mineralogical Society of America.
The published version is subject to change. Cite as Authors (Year) Title. American Mineralogist, in press.
DOI: https://doi.org/10.2138/am-2022-8543. http://www.minsocam.org/

observed in the HRTEM mode. Thus, only the FFT pattern created from the HRTEM image can be used for the phrase identification. The poor crystallinity of these REE phosphates may indicate a rapid crystallization of these REE phosphates from a fluid. Figure 11a shows a La, Nd and Y-bearing phosphate closely attached onto a rod-like halloysite. Figure 11b shows another La, Nd and Y-bearing phosphate with its size of ~200 nm. According to the FFT pattern created from the HRTEM image (Figure 11d), it corresponds to the (110) and (201) plane of the rhabdophane. It thus identified as a nano-sized rhabdophane-(La).

5. Discussion

5.1 Clay mineral features and their effects on rare earth element enrichment

Based on the SEM and TEM observations, the REE-bearing particles are primarily absorbed onto the surfaces of clay minerals (i.e. kaolinite and halloysite), mostly halloysite (Fig. 9 and 11). The HF5–ICP–MS results also support this observation. In the 40–80 nm particle size range, the REE and Al peaks in the HWH sample are only partially coincident after treatment with the TSPP solution ($Na_4P_2O_7$). This indicates that promotion of ion exchange in the aqueous solution led to some REEs being desorbed from the kaolinite surfaces and, as such, the REEs are only weakly adsorbed onto kaolinite. In addition, the absence of a REE peak associated with the particle size range of 40–80 nm in the SWH indicates the REEs have been desorbed from kaolinite. The peaks of the REEs and Al coincide for the particle size range of 5–40 nm in the SWH, indicating that the REEs are still mostly adsorbed onto halloysite after TSPP treatment. Zhou et al. (2022) conducted a similar REE (Eu^{3+}) desorption research from halloysite and kaolinite. The study found that, after exposure into 0.002 mol/L $(NH_4)_2SO_4$ for 24H which is similar to the concentration of the TSPP applied in this study, the desorption amounts of Eu^{3+}

441 from halloysite and kaolinite were 0.10 mol/L and 0.19 mol/L, respectively. These results show
442 that halloysite has a higher REE retention capacity as compared with kaolinite, which may
443 explain the relative loss of REEs in the upper part of the HWH and relative enrichment of REEs
444 in the lower part of the HWH and in the SWH.

445 Kaolinite and halloysite are both 1:1 dioctahedral clay minerals belonging to the kaolinite
446 group (Lázaro 2015). Their adsorption capacity is mainly determined by inner- and outer-sphere
447 complexation of the REEs with the chemically active aluminum hydroxyl (Al–OH) groups,
448 known as aluminol surface (also known as the gibbsite basal plane), which mainly located on the
449 at the edges of platy kaolinite and the internal surface of halloysite (Yang et al. 2019; Borst et al.
450 2020). Fan et al. (2015) observed that Ce nano-particles were wrapped in a hollow halloysite
451 tube in the samples from Zudong ion-adsorption HREE deposit, Jiangxi Province, China using
452 TEM imaging, which provided direct evidence of the surface complexation between the inner
453 surface of halloysite and REEs. In addition to inner- and outer-sphere complexation, a recent
454 study also revealed that REE^{3+} ions penetrated the interlayer of tubular halloysite after
455 immersion in a low-concentration REE solution for three years, whereas this was not the case for
456 kaolinite (Zhou et al. 2021). This was explained by the stronger REE retention capacity of
457 halloysite as compared with kaolinite.

458 Although the siloxane groups exposed at the outer surfaces of kaolinite and halloysite,
459 which show negative zeta potential over a pH range of 2.5 to 8.5, have a weaker affinity for
460 REEs compared to their aluminol surface (Yuan et al. 2008; Tan et al. 2015; Veerabadran et al.
461 2011). Adsorption of REE by the siloxane groups are only involved at the alkaline pH when the
462 aluminol groups are saturated, thus the interaction between REE and siloxane groups was
463 subordinate (Tertre et al. 2006). However, the adsorption of the REEs can be promoted by the

development of surface breakages and defects, which exposes the Al–OH groups and allows isomorphous substitution of the clay structural unit layer (e.g., Al^{3+} for Si^{4+}) on the siloxane surfaces (Joussein et al. 2005; Yuan et al. 2008). Due to its tubular morphology and smaller size, halloysite has a higher specific surface area (SSA) as compared with platy kaolinite, and thus it has more surface defects than kaolinite (Zhou et al. 2022). The isomorphous substitution in halloysite is also reported significant than that in kaolinite (Borst et al. 2020). The Si/Al ratio of the well-ordered kaolinite, poorly ordered kaolinite and halloysite are 1.01, 0.97 and 0.68, suggesting a higher isomorphic substitutions amount of Si by Al in the halloysite (Tarì et al. 1999).

Previous studies have shown that the exposed hydroxyl groups on the alumina and siloxane surfaces on halloysite and kaolinite have variable charges that are pH-dependent (Strawn and Sparks 1999; Laveuf and Cornu 2009). The REE adsorption capacity varies with pH, due to the (de)protonation of hydroxyl groups on the clay surfaces (Bradbury and Baeyens 2002; Tertre et al. 2006). The point zero charge (PZC) of kaolinite is 2.0–4.5, whereas the PZC of halloysite is generally <2 (Kosmulski, 2018, and references therein). Therefore, as the pH increases with depth in the regolith profile, more negatively charged surface sites exist on the halloysite and kaolinite, which thus increase the REE adsorption capacity. As mentioned above, halloysite has a larger SSA than kaolinite and, as such, has more surface functional sites. Experimental studies have revealed that the REE adsorption capacity of clay minerals increases linearly between pH values of 3.0 and 7.5 (Yuan 2018). When pH = 2 and is close to or lower than the PZC of halloysite and kaolinite, the two clay minerals are in a REE-saturated adsorption state, and the REE adsorption capacity is low. When pH = 4, the REE adsorption capacity of the two clay minerals increases more than tenfold, and halloysite has about twice the REE adsorption capacity

This is the peer-reviewed, final accepted version for American Mineralogist, published by the Mineralogical Society of America.
The published version is subject to change. Cite as Authors (Year) Title. American Mineralogist, in press.
DOI: https://doi.org/10.2138/am-2022-8543. http://www.minsocam.org/

487 of kaolinite (Gao et al. 2018; Zhou et al. 2022).

488 In addition, the XRD patterns show that the proportion of halloysite-10Å increases with
489 greater depth in the Dazhou regolith profile (Fig. 6). Halloysite-10Å is mainly developed in the
490 SWH and the lower HWH, which are less weathered parts of the profile, whereas the upper
491 horizons contain higher proportions of kaolinite and halloysite-7Å. This suggests that with
492 progressive weathering, halloysite-10Å was gradually dehydrated and transformed into other
493 kaolinite species. Li and Zhou (2020) documented the irreversible dehydration of metastable
494 halloysite-10Å to halloysite-7Å and subsequent transition to crystalline kaolinite within regolith.
495 The occurrence of hydrated halloysite-10Å is reported to increase the REE adsorption capacity
496 as compared with halloysite-7Å (Ram et al. 2019). The greater cation exchange capacity of
497 halloysite-10Å as compared with halloysite-7Å and kaolinite is attributed to the more extensive
498 substitutions of Al^{3+} for Si^{4+} occurred in the tetrahedral sheet of halloysite-10Å (Kautz and Ryan
499 2003; Joussein et al. 2005). As such, more REEs occur in the halloysite-10Å-rich layers in the
500 regolith.

501

502 **5.2 Occurrence of rare earth element nano-particles**

503 The δCe and ΣREE contents indicate that Ce is enriched in the upper horizons (δCe >2,
504 ΣREE_{max}= 208.14 ppm, FWH) and depleted in the lower horizons (δCe <1, ΣREE_{max}= 984.17
505 and 1201.01 ppm, HWH and SWH) of the profile, with the latter being enriched in the other
506 REEs (Fig. 3). This reflects the loss of the REEs, apart from Ce, from the upper horizons, due to
507 chemical leaching and weathering. The SEM and TEM observations are consistent with the
508 geochemical data, whereby Ce was observed as Ce-oxide and Ce-silicate in the upper horizons,
509 whereas other REEs (La, Nd, and Y) were observed as secondary REE phosphates with poor

crystallinity in the lower horizons. EDS analyses of these REE phosphates revealed they are Ce-depleted (Ce less than 1% wt%, below the detection limit of the EDS), indicating that Ce fractionation from the other REEs occurred in the upper horizons. These particle phases are mainly hosted by clay minerals (halloysite and kaolinite).

The anomalous behavior of Ce can be attributed to the different chemical properties of Ce as compared with the other REEs (Compton et al. 2003). Under near-surface oxidizing conditions, Ce^{3+} is rapidly oxidized to Ce^{4+}, and occurs mainly as insoluble Ce oxides or oxyhydroxides. As such, the formation of secondary Ce phases reduces the mobility of Ce and results in the positive Ce anomalies in the upper part of the regolith (Estrade et al. 2014; Janots et al. 2015; Ram et al. 2019; Denys et al. 2021).The other REEs have similar geochemical properties, and occur mainly as REE^{3+}. The REE^{3+} are readily leached by fluids in the upper part of the regolith profile, and then become enriched in the lower part of the profile (Taunton et al. 2000b).

Secondary phosphate can readily form by interface precipitation with REEs on mineral surfaces (Patel et al. 2017; Kashiwabara et al. 2018). The formation of REE phosphates involves the dissolution of primary REE-bearing phosphate (e.g., xenotime, monazite, and apatite), and the precipitation of REE phosphate (Ichimura et al. 2020; Voutsinos et al. 2021). Common LREE-bearing secondary phosphate mineral phases in the weathering environment include churchite ($Y(PO_4)\cdot 2H_2O$), rhabdophane ((Ce, Y, La, etc.,)$(PO_4)\cdot H_2O$), and florencite ($CeAl_3(PO_4)_2(OH)_6$). Several studies have observed the precipitation of secondary rhabdophane and florencite directly onto the surface of primary apatite during its dissolution (Banfield and Eggleton 1989; Taunton et al. 2000b; Voutsinos et al. 2021). Secondary REE phosphate minerals generally have a very low solubility ($K_{SP} = 10^{-24.5}$) (Byrne and Kim, 1993; Liu and Byrne, 1997).

This is the peer-reviewed, final accepted version for American Mineralogist, published by the Mineralogical Society of America.
The published version is subject to change. Cite as Authors (Year) Title. American Mineralogist, in press.
DOI: https://doi.org/10.2138/am-2022-8543. http://www.minsocam.org/

533 However, the secondary REE phosphates were only observed on the surfaces of primary REE
534 phosphates from the incipient weathering zone, although these secondary REE phosphates are
535 thought to be highly insoluble (Braun et al. 1998; Taunton et al. 2000b). The SEM and TEM
536 observations also suggest that secondary REE phosphates are absent from the uppermost
537 horizons, which is consistent with these previous studies. This may indicate that the secondary
538 REE phosphates in the uppermost horizons were leached downward as weathering proceeded to
539 greater depths.

540 **5.3 Controls on rare earth element mobilization and fractionation**

541 Like most metallic elements, the solubility of the REEs and REE phosphates increases with
542 decreasing pH (Valsami-Jones et al. 1998; Cetiner et al. 2005). The dissolution rate of primary
543 REE phosphates increases with decreasing pH, and the dissolution rate at pH = 5 ($\sim 5.14\times10^{-10}$
544 mol m^{-2} s^{-1}) is about one order of magnitude higher than at pH = 6 ($\sim 5.69\times10^{-11}$ mol m^{-2} s^{-1})
545 (Guidry and Mackenzie 2003). Therefore, the primary REE phosphates were rapidly weathered,
546 which released REE^{3+} and PO_4^{3-} into the associated fluids. Despite its low solubility, secondary
547 REE phosphates are rare in highly weathered horizons (Braun et al. 1998; Taunton et al. 2000b;
548 Ichimura et al. 2020). Köhler et al. (2005) reported that aqueous Nd concentrations in
549 equilibrium with rhabdophane increased from a few tens of ppt to ~10,000 ppt when the pH
550 decreased from 5.5 to 4.5, in the presence of aqueous Ca^{2+}, PO_4^{3-}, and F^- with concentrations of
551 10^{-4}, 10^{-5}, and 5×10^{-7} mol/kg, respectively. These conditions are typical of slightly acidic fluids
552 in near-surface soils. The mean pH of the FWH is 5.07, and thus it can be speculated that the
553 formation of secondary REE phosphates was inhibited or the newly formed REE phosphates
554 were rapidly dissolved in the surface environment (Fig. 3). In addition, Nd concentrations of a
555 few tens of ppt to <10 ppt are supersaturated for solutions with pH = 5.5–6.5, which is similar to

556 the pH of the lower horizons (i.e., the lower part of the HWH and the SWH). The low pH in the
557 upper horizons favored the weathering, dissolution, and migration of the REEs, whereas the
558 elevated pH in the lower horizons promoted the re-precipitation of the REEs.

559 Microbial uptake is also a key aspect in the enrichment and leaching of REEs in a regolith
560 profile (Johannesson et al. 2004; Tyler 2004; Ma et al. 2011). Fu et al. (2019) reported that the
561 soil organic matter (SOM) and organic-bound REE concentrations decreased from the uppermost
562 to lower horizons in regolith in the Darongshan region. There is a significant increase in loss-on-
563 ignition values towards the surface, indicative of the accumulation of microorganisms and SOM
564 in the uppermost horizons (Fig. 3), which are negatively correlated with ΣREE contents.
565 Microbial activity is considered to accelerate rock weathering by acidolysis, complexolysis, and
566 redoxolysis processes in the surface horizons, including of primary phosphate minerals, which
567 promotes the release of $REE^{3+/4+}$ into solutions in soils (Taunton et al. 2000a; Brandl 2001). In
568 addition, secondary REE phosphate surfaces have been observed to be coated by microbes in
569 relict primary REE phosphate pits, indicating the uptake of phosphate by organisms (Taunton et
570 al. 2000b; Welch et al. 2002). SOM is negatively charged and can strongly absorb and/or chelate
571 to REE cations (Wu et al. 2001). The complexation of SOM and $REE^{3+/4+}$ further enhances the
572 adsorption of REEs onto the surfaces of Fe–Mn oxyhydroxides and clay minerals, which is
573 important for the mobility and transport of REEs in a regolith (Davranche et al. 2008). Our HF5–
574 ICP–MS results identified significant loss of fine clay particles in the upper horizons of the
575 Dazhou regolith profile (Fig. 8). These fine-grained clays with a higher REE adsorption capacity
576 accumulated in the lower horizons. Therefore, the OM-rich upper horizons acted as an effective
577 barrier to the formation of secondary REE phosphates and limited the REE enrichment in these
578 horizons.

579

580 ## 6 Implications

581 This study has shown how chemical weathering, clay mineralogy, and secondary REE nano-
582 particles and nano-minerals affect the fractionation and enrichment of REEs in granite regolith.
583 There are differences in the clay mineral type, content, and grain size between the upper and
584 lower horizons. The upper horizons have lost fine-grained clays and consist mainly of platy
585 kaolinite, whereas the proportion of tubular halloysite increases with depth. Compared with the
586 platy kaolinite, the halloysite is smaller, and thus has a higher SSA and CEC that enhances REE
587 adsorption and enrichment. As a result, the REEs remain adsorbed and enriched in the lower part
588 of the HWH and in the SWH in the Dazhou granite regolith.

589 The development of this REE-rich granite regolith was closely related to the formation of
590 secondary REE phosphates and oxides. Significant REE fractionation is the result of weathering
591 of primary minerals and the formation of secondary REE-bearing particles. Previous studies have
592 shown that, compared with regolith with low P_2O_5 contents, regolith with high P_2O_5 contents
593 contains a large amount of secondary REE phosphates (Bern et al. 2017). Moreover, the P_2O_5
594 contents are negatively correlated with the ion-exchangeable REE contents (Sanematsu et al.
595 2015; Bern et al. 2017). The formation of cerite in the upper horizons causes Ce depletion in the
596 lower horizons, which has been widely documented in previous studies of weathering profiles
597 (Compton et al. 2003; Ma et al. 2011; Fu et al. 2019). The fractionation of secondary REE-
598 bearing particles was due to chemical leaching and changing geochemical conditions in the
599 profile. The formation of secondary REE minerals is clearly critical to the development of ion
600 adsorption-type REE deposits.

601 A recent study has shown that the traditional sequential extraction method, which had been

602 widely used in REE speciation studies of regolith, may lead to inaccurate results due to the use of
603 hydroxylamine hydrochloride (HaH; NH_2OH,HCl) in the Mn oxide speciation step (Denys et al.
604 2021). The use of HaH may lead to Ce being adsorbed onto the surfaces of Mn and Fe
605 oxyhydroxides and partial dissolution of REE phosphates and carbonates, which compromises
606 the REE speciation data. With further improvements in the selective extraction procedure, more
607 authigenic REE phosphate phases are expected to be identified. Therefore, in addition to cation-
608 exchange fractionation of the REEs, the formation of secondary REE nano-particles likely results
609 in REE fractionation and enrichment in granite regolith. These secondary REE-bearing nano-
610 particles or nano-minerals may have a larger role in supergene REE enrichment than previously
611 thought.
612

613 **Acknowledgments**

614 This research was financially supported by the National Natural Science Foundation of
615 China (91962107; 42173067; 42003066), Guangxi Natural Science Foundation
616 (2020GXNSFGA297003, 2019AC20007) and the project of Collaborative Innovation Center for
617 Exploration of Hidden Nonferrous Metal Deposits and Development of New Materials in
618 Guangxi.
619

620 ## References
621
622 Andrade, F.R.D. de, Polo, L.A., Janasi, V. de A., and Carvalho, F.M. de S. (2018) Volcanic glass in Cretaceous
623 dacites and rhyolites of the Paraná Magmatic Province, southern Brazil: Characterization and
624 quantification by XRD-Rietveld. Journal of Volcanology and Geothermal Research, 355, 219–231.

625 Baalousha, M., Prasad, A., and Lead, J.R. (2014) Quantitative measurement of the nanoparticle size and
626 number concentration from liquid suspensions by atomic force microscopy. Environmental Science:
627 Processes & Impacts, 16, 1338–1347.

628 Banfield, J.F., and Eggleton, R.A. (1989) Apatite Replacement and Rare Earth Mobilization, Fractionation, and
629 Fixation During Weathering. Clays and Clay Minerals, 37, 113–127.

630 Bao, Z.W., and Zhao, Z.H. (2008) Geochemistry of mineralization with exchangeable REY in the weathering
631 crusts of granitic rocks in South China. Ore Geology Reviews, 33, 519–535.

632 Berger, A., Janots, E., Gnos, E., Frei, R., and Bernier, F. (2014) Rare earth element mineralogy and
633 geochemistry in a laterite profile from Madagascar. Applied Geochemistry, 41, 218–228.

634 Bern, C.R., Yesavage, T., and Foley, N.K. (2017) Ion-adsorption REEs in regolith of the Liberty Hill pluton,
635 South Carolina, USA: An effect of hydrothermal alteration. Journal of Geochemical Exploration, 172,
636 29–40.

637 Borst, A.M., Smith, M.P., Finch, A.A., Estrade, G., Villanova-de-Benavent, C., Nason, P., Marquis, E.,
638 Horsburgh, N.J., Goodenough, K.M., Xu, C., and others (2020) Adsorption of rare earth elements in
639 regolith-hosted clay deposits. Nature Communications, 11, 4386.

640 Bradbury, M.H., and Baeyens, B. (2002) Sorption of Eu on Na- and Ca-montmorillonites: experimental
641 investigations and modelling with cation exchange and surface complexation. Geochimica et
642 Cosmochimica Acta, 66, 2325–2334.

643 Brandl, H. (2001) Microbial leaching of metals. Biotechnology, 10, 191–224.

644 Braun, J.-J., Viers, J., Dupré, B., Polve, M., Ndam, J., and Muller, J.-P. (1998) Solid/Liquid REE Fractionation
645 in the Lateritic System of Goyoum, East Cameroon: The Implication for the Present Dynamics of the
646 Soil Covers of the Humid Tropical Regions. Geochimica et Cosmochimica Acta, 62, 273–299.

647 Cetiner, Z.S., Wood, S.A., and Gammons, C.H. (2005) The aqueous geochemistry of the rare earth elements.
648 Part XIV. The solubility of rare earth element phosphates from 23 to 150 °C. Chemical Geology, 217,
649 147–169.

650 Chakhmouradian, A.R., and Wall, F. (2012) Rare Earth Elements: Minerals, Mines, Magnets (and More).
651 Elements, 8, 333–340.

652 Chen, C.H., Hsieh, P.S., Lee, C.Y., and Zhou, H.W. (2011) Two episodes of the Indosinian thermal event on the
653 South China Block: Constraints from LA-ICPMS U–Pb zircon and electron microprobe monazite ages
654 of the Darongshan S-type granitic suite. Gondwana Research, 19, 1008–1023.

655 Chen, T.H., Xie, Q.Q., Xu, H., Chen, J., Ji, J.F., Lu, H.Y., and Balsam, W. (2010) Characteristics and formation
656 mechanism of pedogenic hematite in Quaternary Chinese loess and paleosols. Catena, 81, 217–225.

657 Christian, P., Kammer, F.V. der, Baalousha, M., and Hofmann, T. (2008) Nanoparticles: structure, properties,
658 preparation and behaviour in environmental media. Ecotoxicology, 17, 326–343.

Ciobanu, C.L., Cook, N.J., Utsunomiya, S., Pring, A., and Green, L. (2011) Focussed ion beam–transmission electron microscopy applications in ore mineralogy: Bridging micro- and nanoscale observations. Ore Geology Reviews, 42, 6–31.

Ciobanu, C.L., Cook, N.J., Utsunomiya, S., Kogagwa, M., Green, L., Gilbert, S., and Wade, B. (2012) Gold-telluride nanoparticles revealed in arsenic-free pyrite. American Mineralogist, 97, 1515–1518.

Coelho, A.A. (2018) TOPAS and TOPAS-Academic: an optimization program integrating computer algebra and crystallographic objects written in C++. Journal of Applied Crystallography, 51, 210–218.

Compton, J.S., White, R.A., and Smith, M. (2003) Rare earth element behavior in soils and salt pan sediments of a semi-arid granitic terrain in the Western Cape, South Africa. Chemical Geology, 201, 239–255.

Davranche, M., Pourret, O., Gruau, G., Dia, A., Jin, D., and Gaertner, D. (2008) Competitive binding of REE to humic acid and manganese oxide: Impact of reaction kinetics on development of cerium anomaly and REE adsorption. Chemical Geology, 247, 154–170.

Deditius, A.P., Utsunomiya, S., Reich, M., Kesler, S.E., Ewing, R.C., Hough, R., and Walshe, J. (2011) Trace metal nanoparticles in pyrite. Ore Geology Reviews, 42, 32–46.

Degen, T., Sadki, M., Bron, E., König, U., and Nénert, G. (2014) The HighScore suite. Powder Diffraction, 29, S13–S18.

Denys, A., Janots, E., Auzende, A.-L., Lanson, M., Findling, N., and Trcera, N. (2021) Evaluation of selectivity of sequential extraction procedure applied to REE speciation in laterite. Chemical Geology, 559, 119954.

Estrade, G., Béziat, D., Salvi, S., Tiepolo, M., Paquette, J.-L., and Rakotovao, S. (2014) Unusual evolution of silica-under- and -oversaturated alkaline rocks in the Cenozoic Ambohimirahavavy Complex (Madagascar): Mineralogical and geochemical evidence. Lithos, 206–207, 361–383.

Estrade, G., Marquis, E., Smith, M., Goodenough, K., and Nason, P. (2019) REE concentration processes in ion adsorption deposits: Evidence from the Ambohimirahavavy alkaline complex in Madagascar. Ore Geology Reviews, 112, 103027.

Fan, C.Z., Zhang, Y., Chen, Z.H., Zhu, Y., and Fan, X.T. (2015) The study of clay minerals from weathered crust rare earth ores in southern Jiangxi Province. Acta Petrologica et Mineralogica, 34, 803–810 (in Chinese with English abstract).

Fu, W., Li, X.T., Feng, Y.Y., Feng, M., Peng, Z., Yu, H.X., and Lin, H. (2019) Chemical weathering of S-type granite and formation of Rare Earth Element (REE)-rich regolith in South China: Critical control of lithology. Chemical Geology, 520, 33–51.

Gao, Y.H., Fan, C.Z., Xu, H., and Wang, L. (2018) An experimental study of the characteristics of REE adsorption of kaolinite and halloysite-7Å. Acta Petrologica et Mineralogica, 37, 161–168 (in Chinese with English abstract).

Guidry, M.W., and Mackenzie, F.T. (2003) Experimental study of igneous and sedimentary apatite dissolution: Control of pH, distance from equilibrium, and temperature on dissolution rates. Geochimica et Cosmochimica Acta, 67, 2949–2963.

Gulley, A.L., Nassar, N.T., and Xun, S. (2018) China, the United States, and competition for resources that enable emerging technologies. Proceedings of the National Academy of Sciences, 115, 4111–4115.

Hill, R.J., and Howard, C.J. (1987) Quantitative phase analysis from neutron powder diffraction data using the Rietveld method. Journal of Applied Crystallography, 20, 467–474.

Hochella, M.F. (2008) Nanogeoscience: from origins to cutting-edge applications. Elements, 4, 373–379.

Hough, R.M., Noble, R.R.P., and Reich, M. (2011) Natural gold nanoparticles. Ore Geology Reviews, 42, 55–61.

Huo, M.Q., Sun, Q., Bai, Y.H., Xie, P., Liu, Z.R., Li, J.H., Wang, X.S., and Lu, S.H. (2011) Chemical character of precipitation and related particles and trace gases in the North and South of China. Journal of Atmospheric Chemistry, 67, 29.

Ichimura, K., Sanematsu, K., Kon, Y., Takagi, T., and Murakami, T. (2020) REE redistributions during granite weathering: Implications for Ce anomaly as a proxy for paleoredox states. American Mineralogist, 105, 848–859.

Janots, E., Bernier, F., Brunet, F., Muñoz, M., Trcera, N., Berger, A., and Lanson, M. (2015) Ce(III) and Ce(IV) (re)distribution and fractionation in a laterite profile from Madagascar: Insights from in situ XANES spectroscopy at the Ce LIII-edge. Geochimica et Cosmochimica Acta, 153, 134–148.

jEdit (2022) jEdit - Programmer's Text Editor - overview. http://www.jedit.org/index.php (accessed 15 August 2022).

Jiao, S.J., Li, X.H., Huang, H.Q., and Deng, X.G. (2015) Metasedimentary melting in the formation of charnockite: Petrological and zircon U-Pb-Hf-O isotope evidence from the Darongshan S-type granitic complex in southern China. Lithos, 239, 217–233.

Johannesson, K.H., Tang, J., Daniels, J.M., Bounds, W.J., and Burdige, D.J. (2004) Rare earth element concentrations and speciation in organic-rich blackwaters of the Great Dismal Swamp, Virginia, USA. Chemical Geology, 209, 271–294.

Joussein, E., Petit, S., Churchman, J., Theng, B., Righi, D., and Delvaux, B. (2005) Halloysite clay minerals — a review. Clay Minerals, 40, 383–426.

Kashiwabara, T., Toda, R., Nakamura, K., Yasukawa, K., Fujinaga, K., Kubo, S., Nozaki, T., Takahashi, Y., Suzuki, K., and Kato, Y. (2018) Synchrotron X-ray spectroscopic perspective on the formation mechanism of REY-rich muds in the Pacific Ocean. Geochimica et Cosmochimica Acta, 240, 274–292.

Kautz, C.Q., and Ryan, P.C. (2003) The 10 Å to 7 Å Halloysite Transition in a Tropical Soil Sequence, Costa Rica. Clays and Clay Minerals, 51, 252–263.

Köhler, S.J., Harouiya, N., Chaïrat, C., and Oelkers, E.H. (2005) Experimental studies of REE fractionation during water–mineral interactions: REE release rates during apatite dissolution from pH 2.8 to 9.2. Chemical Geology, 222, 168–182.

Kosmulski, M. (2018) The pH dependent surface charging and points of zero charge. VII. Update. Advances in Colloid and Interface Science, 251, 115–138.

Kynicky, J., Smith, M.P., and Xu, C. (2012) Diversity of Rare Earth Deposits: The Key Example of China. Elements, 8, 361–367.

Laveuf, C., and Cornu, S. (2009) A review on the potentiality of Rare Earth Elements to trace pedogenetic

processes. Geoderma, 154, 1–12.

Lázaro, B.B. (2015) Halloysite and kaolinite: two clay minerals with geological and technological importance. Revista de la Academia de Ciencias Exactas, Físicas, Químicas y Naturales de Zaragoza, 7–38.

Li, M.Y.H., and Zhou, M.F. (2020) The role of clay minerals in formation of the regolith-hosted heavy rare earth element deposits. American Mineralogist, 105, 92–108.

Li, P.C. (2014) The study of mineralization and origin of rock mass and ion-adsorbed rare earth ore in Liuchen Guangxi. Sichuan Nonferrous Metals, 23–27 (in Chinese with English abstract).

Li, X.Y. (2020) Geological characteristics and metallogenic condition of Shanglong REE deposit in Pingnan County of Guangxi. Mineral Resources and Geology, 34, 704–709 (in Chinese with English abstract).

Li, Y.H.M., Zhao, W.W., and Zhou, M.F. (2017) Nature of parent rocks, mineralization styles and ore genesis of regolith-hosted REE deposits in South China: An integrated genetic model. Journal of Asian Earth Sciences, 148, 65–95.

Liu, R., Wang, R.C., Lu, X.C., and Li, J. (2016) Nano-sized rare earth minerals from granite-related weathering-type REE deposits in southern Jiangxi. Acta Petrologica et Mineralogica, 35, 617–626 (in Chinese with English abstract).

Ma, L., Jin, L.X., and Brantley, S.L. (2011) How mineralogy and slope aspect affect REE release and fractionation during shale weathering in the Susquehanna/Shale Hills Critical Zone Observatory. Chemical Geology, 290, 31–49.

Min, M.Z., Kong, L.F., and Zhang, G.W. (1995) Isotope geochemistry of the Liuchen granite, Guangxi province. Geological Review, 41, 48–51 (in Chinese with English abstract).

Mukai, H., Kon, Y., Sanematsu, K., Takahashi, Y., and Ito, M. (2020) Microscopic analyses of weathered granite in ion-adsorption rare earth deposit of Jianxi Province, China. Scientific Reports, 10, 20194.

Palenik, C.S., Utsunomiya, S., Reich, M., Kesler, S.E., Wang, L.M., and Ewing, R.C. (2004) “Invisible” gold revealed: direct imaging of gold nanoparticles in a Carlin-type deposit. American Mineralogist, 89, 1359–1366.

Patel, M.A., Kar, A.S., Kumar, S., and Tomar, B.S. (2017) Effect of phosphate on sorption of Eu(III) by montmorillonite. Journal of Radioanalytical and Nuclear Chemistry, 313, 537–545.

Prasad, A., Lead, J.R., and Baalousha, M. (2015) An electron microscopy based method for the detection and quantification of nanomaterial number concentration in environmentally relevant media. Science of The Total Environment, 537, 479–486.

Ram, R., Becker, M., Brugger, J., Etschmann, B., Burcher-Jones, C., Howard, D., Kooyman, P.J., and Petersen, J. (2019) Characterisation of a rare earth element- and zirconium-bearing ion-adsorption clay deposit in Madagascar. Chemical Geology, 522, 93–107.

Regelink, I.C., Weng, L.P., Koopmans, G.F., and van Riemsdijk, W.H. (2013) Asymmetric flow field-flow fractionation as a new approach to analyse iron-(hydr)oxide nanoparticles in soil extracts. Geoderma, 202–203, 134–141.

Rietveld, H.M. (2014) The rietveld method. Physica Scripta, 89, 098002.

Sanematsu, K., and Watanabe, Y. (2016) Characteristics and Genesis of Ion Adsorption-Type Rare Earth Element Deposits. In Rare Earth and Critical Elements in Ore Deposits. Society of Economic Geologists.

Sanematsu, K., Kon, Y., Imai, A., Watanabe, K., and Watanabe, Y. (2013) Geochemical and mineralogical characteristics of ion-adsorption type REE mineralization in Phuket, Thailand. Mineralium Deposita, 48, 437–451.

Sanematsu, K., Kon, Y., and Imai, A. (2015) Influence of phosphate on mobility and adsorption of REEs during weathering of granites in Thailand. Journal of Asian Earth Sciences, 111, 14–30.

Schindler, M., and Hochella, M.F. (2015) Soil memory in mineral surface coatings: Environmental processes recorded at the nanoscale. Geology, 43, 415–418.

——— (2016) Nanomineralogy as a new dimension in understanding elusive geochemical processes in soils: The case of low-solubility-index elements. Geology, 44, 515–518.

Schindler, M., Michel, S., Batcheldor, D., and Hochella, M.F. (2019) A nanoscale study of the formation of Fe-(hydr)oxides in a volcanic regolith: Implications for the understanding of soil forming processes on Earth and Mars. Geochimica et Cosmochimica Acta, 264, 43–66.

Schulz, K.J., DeYoung, J.H., Seal, R.R., and Bradley, D.C. (2018) Critical Mineral Resources of the United States: Economic and Environmental Geology and Prospects for Future Supply. Geological Survey.

Siripinyanond, A., M. Barnes, R., and Amarasiriwardena, D. (2002) Flow field-flow fractionation- inductively coupled plasma mass spectrometry for sediment bound trace metal characterization. Journal of Analytical Atomic Spectrometry, 17, 1055–1064.

Sonneveld, E.J., and Visser, J.W. (1975) Automatic collection of powder data from photographs. Journal of Applied Crystallography, 8, 1–7.

Stolpe, B., Guo, L., and Shiller, A.M. (2013) Binding and transport of rare earth elements by organic and iron-rich nanocolloids in Alaskan rivers, as revealed by field-flow fractionation and ICP-MS. Geochimica et Cosmochimica Acta, 106, 446–462.

Strawn, D.G., and Sparks, D.L. (1999) The Use of XAFS to Distinguish between Inner- and Outer-Sphere Lead Adsorption Complexes on Montmorillonite. Journal of Colloid and Interface Science, 216, 257–269.

Sun, M.H., Wang, Y., Wang, T., Fan, S.J., Wang, W.X., Li, P.H., Guo, J., and Li, Y.H. (2010) Cloud and the corresponding precipitation chemistry in south China: Water-soluble components and pollution transport. Journal of Geophysical Research: Atmospheres, 115.

Tan, D.Y., Yuan, P., Annabi-Bergaya, F., Dong, F.Q., Liu, D., and He, H.P. (2015) A comparative study of tubular halloysite and platy kaolinite as carriers for the loading and release of the herbicide amitrole. Applied Clay Science, 114, 190–196.

Tan, Z.Q., Liu, J.F., Guo, X.R., Yin, Y.G., Byeon, S.K., Moon, M.H., and Jiang, G.-B. (2015) Toward Full Spectrum Speciation of Silver Nanoparticles and Ionic Silver by On-Line Coupling of Hollow Fiber Flow Field-Flow Fractionation and Minicolumn Concentration with Multiple Detectors. Analytical Chemistry, 87, 8441–8447.

Tarì, G., Bobos, I., Gomes, C.S.F., and Ferreira, J.M.F. (1999) Modification of Surface Charge Properties

812 during Kaolinite to Halloysite-7Å Transformation. Journal of Colloid and Interface Science, 210, 360–
813 366.

814 Taunton, A.E., Welch, S.A., and Banfield, J.F. (2000a) Geomicrobiological controls on light rare earth element,
815 Y and Ba distributions during granite weathering and soil formation. Journal of Alloys and
816 Compounds, 303–304, 30–36.

817 ——— (2000b) Microbial controls on phosphate and lanthanide distributions during granite weathering and
818 soil formation. Chemical Geology, 169, 371–382.

819 Tertre, E., Berger, G., Simoni, E., Castet, S., Giffaut, E., Loubet, M., and Catalette, H. (2006) Europium
820 retention onto clay minerals from 25 to 150°C: Experimental measurements, spectroscopic features
821 and sorption modelling. Geochimica et Cosmochimica Acta, 70, 4563–4578.

822 Tyler, G. (2004) Rare earth elements in soil and plant systems - A review. Plant and Soil, 267, 191–206.

823 Valsami-Jones, E., Ragnarsdottir, K.V., Putnis, A., Bosbach, D., Kemp, A.J., and Cressey, G. (1998) The
824 dissolution of apatite in the presence of aqueous metal cations at pH 2–7. Chemical Geology, 151,
825 215–233.

826 Veerabadran, N.G., PRICE, R.R., and Lvov, Y.M. (2011) Clay nanotubes for encapsulation and sustained
827 release of drugs. NANO.

828 Voutsinos, M.Y., Banfield, J.F., and Moreau, J.W. (2021) Secondary lanthanide phosphate mineralisation in
829 weathering profiles of I-, S- and A-type granites. Mineralogical Magazine, 85, 82–93.

830 Wang, S. (1991) Characteristics and genesis of granitoids in the Darongshan and Shiwandashan area of
831 Guangxi Province, China. Acta Petrologica Sinica, 5, 73–80.

832 Welch, S.A., Taunton, A.E., and Banfield, J.F. (2002) Effect of microorganisms and microbial metabolites on
833 apatite dissolution. Geomicrobiology Journal, 19, 343–367.

834 Wu, C.Y., Huang, D.H., and Guo, Z.X. (1990) REE Geochemistry in the Weathered Crust of Granites,
835 Longnan Area, Jiangxi Province. Acta Geologica Sinica - English Edition, 3, 193–209.

836 Wu, Z.H., Luo, J., Guo, H.Y., Wang, X.R., and Yang, C.S. (2001) Adsorption isotherms of lanthanum to soil
837 constituents and effects of pH, EDTA and fulvic acid on adsorption of lanthanum onto goethite and
838 humic acid. Chemical Speciation & Bioavailability, 13, 75–81.

839 Xu, C., Kynický, J., Smith, M.P., Kopriva, A., Brtnický, M., Urubek, T., Yang, Y., Zhao, Z., He, C., and Song,
840 W. (2017) Origin of heavy rare earth mineralization in South China. Nature Communications, 8, 1–7.

841 Yang, M.J., Liang, X.L., Ma, L.Y., Huang, J., He, H.P., and Zhu, J. (2019) Adsorption of REEs on kaolinite and
842 halloysite: A link to the REE distribution on clays in the weathering crust of granite. Chemical
843 Geology, 525, 210–217.

844 Yi, Z.B., Loosli, F., Wang, J.J., Berti, D., and Baalousha, M. (2020) How to distinguish natural versus
845 engineered nanomaterials: insights from the analysis of TiO_2 and CeO_2 in soils. Environmental
846 Chemistry Letters, 18, 215–227.

847 Yuan, P. (2018) Unique structure and surface-interface reactivity of nanostructured minerals. Earth Sci, 43,
848 1384.

Yuan, P., Southon, P.D., Liu, Z.W., Green, M.E.R., Hook, J.M., Antill, S.J., and Kepert, C.J. (2008) Functionalization of Halloysite Clay Nanotubes by Grafting with γ-Aminopropyltriethoxysilane. The Journal of Physical Chemistry C, 112, 15742–15751.

Yudovskaya, M.A., Distler, V.V., Chaplygin, I.V., Mokhov, A.V., Trubkin, N.V., and Gorbacheva, S.A. (2006) Gaseous transport and deposition of gold in magmatic fluid: evidence from the active Kudryavy volcano, Kurile Islands. Mineralium Deposita, 40, 828.

Yusoff, Z.M., Ngwenya, B.T., and Parsons, I. (2013) Mobility and fractionation of REEs during deep weathering of geochemically contrasting granites in a tropical setting, Malaysia. Chemical Geology, 349–350, 71–86.

Zhou, J.M., Yuan, P., Yu, L., Liu, X.Y., Zhang, B.F., Fan, W.X., and Liu, D. (2018) Mineralogical characteristics of fine particles of the tuff weathering crust from the Bachi rare earth element (REE) deposit. Acta Mineralogica Sinica, 38, 420–428 (in Chinese with English abstract).

Zhou, J.M., Li, M.Y., Yuan, P., Li, Y., Liu, H., Fan, W.X., Liu, D., and Zhang, H. (2021) Partial rehydration of tubular halloysite (7 Å) immersed in La(NO3)3 solution for 3 years and its implication for understanding REE occurrence in weathered crust elution-deposited rare earth ores. Applied Clay Science, 213, 106244.

Zhou, J.M., Liu, H.M., Liu, D., Yuan, P., Bu, H.L., Du, P.X., Fan, W.X., and Li, M.Y. (2022) Sorption/desorption of Eu(III) on halloysite and kaolinite. Applied Clay Science, 216, 106356.

This is the peer-reviewed, final accepted version for American Mineralogist, published by the Mineralogical Society of America.
The published version is subject to change. Cite as Authors (Year) Title. American Mineralogist, in press.
DOI: https://doi.org/10.2138/am-2022-8543. http://www.minsocam.org/

Figure Caption

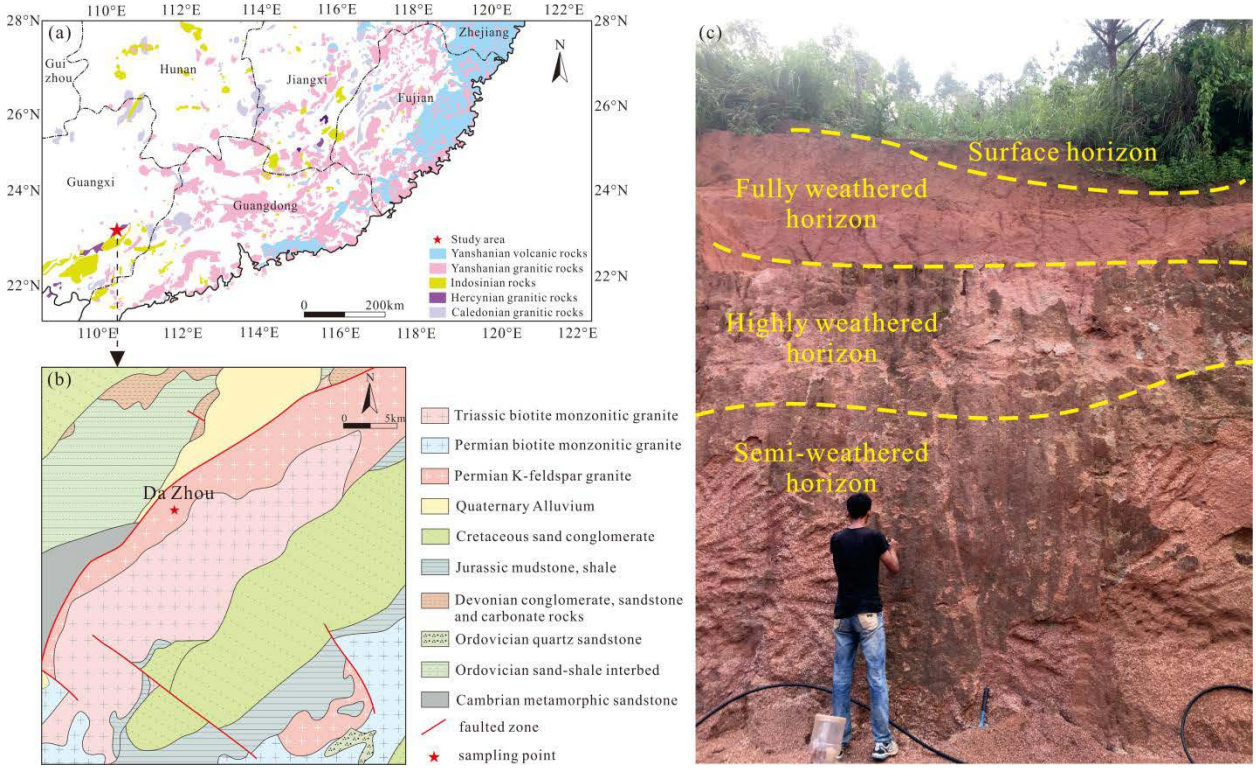

Figure 1. (a) Simplified map showing the distribution of granitic rocks in South China, and the sampling locations of the Dazhou batholith. (b) Simplified geological map of the study area, showing the sampling locations of the regolith profiles. (c) Photograph of a weathering profile.

This is the peer-reviewed, final accepted version for American Mineralogist, published by the Mineralogical Society of America.
The published version is subject to change. Cite as Authors (Year) Title. American Mineralogist, in press.
DOI: https://doi.org/10.2138/am-2022-8543. http://www.minsocam.org/

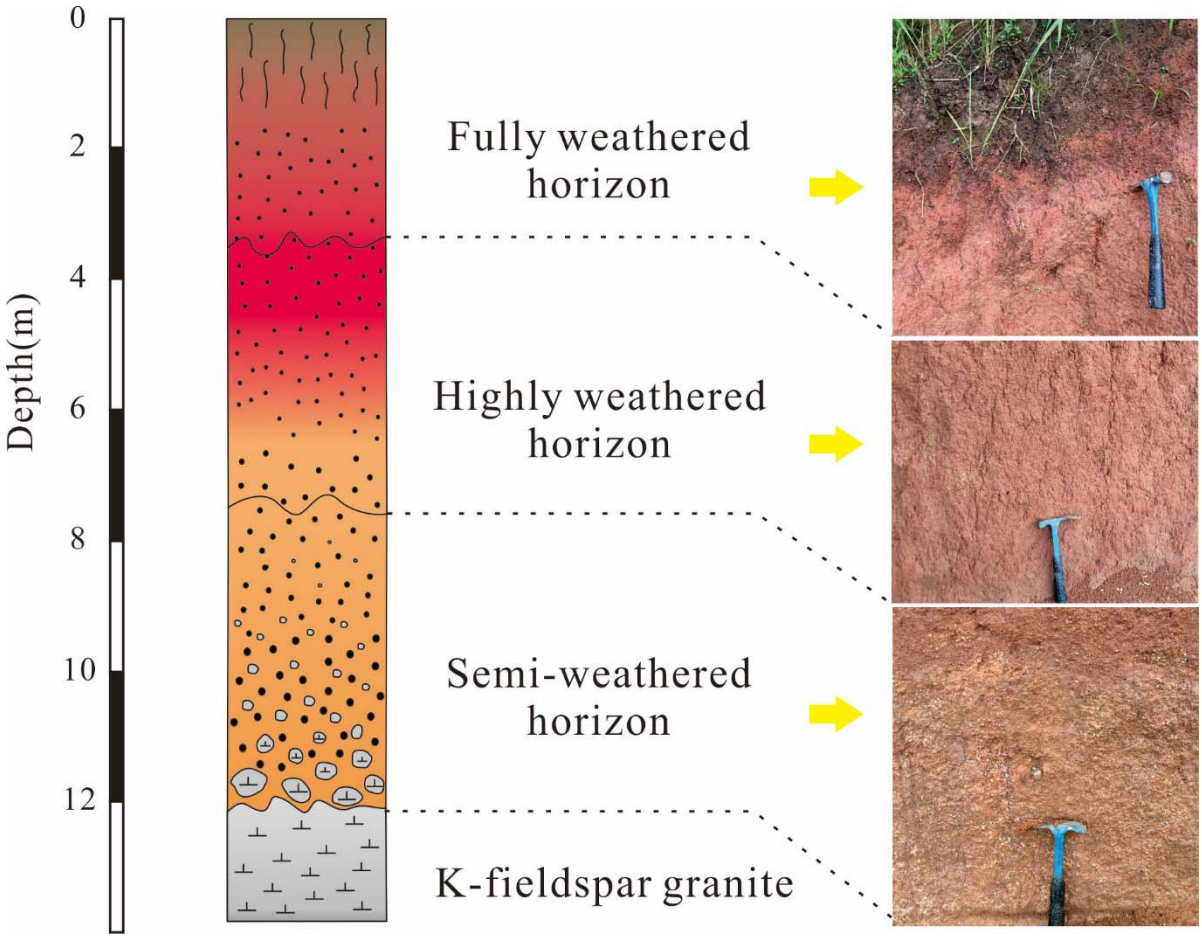

878
879 **Figure 2.** Representative weathering profile for the batholith of the Dazhou, showing the sample locations and
880 lithostratigraphic units.
881
882
883
884
885

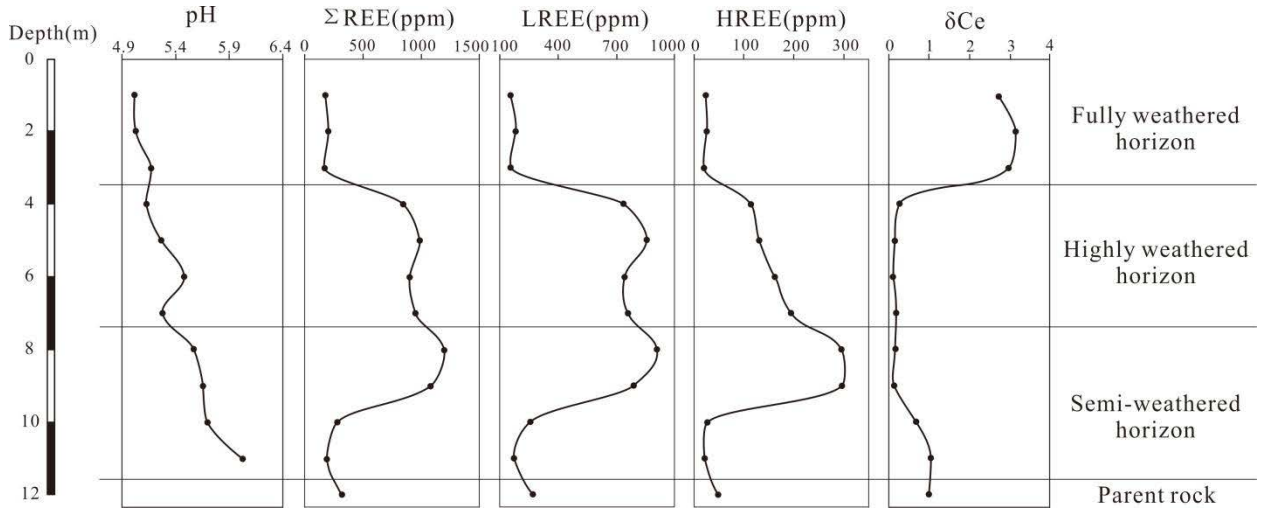

Figure 3. Variations in ΣREE, LREE, HREE, δCe, and pH values in the weathering profiles developed on the Dazhou batholith. Notes: LREE= La, Ce, Pr, Nd, Pm, Sm, Eu and Gd; HREE= Tb, Dy, Ho, Er, Tm, Yb, Lu and Y.

This is the peer-reviewed, final accepted version for American Mineralogist, published by the Mineralogical Society of America.
The published version is subject to change. Cite as Authors (Year) Title. American Mineralogist, in press.
DOI: https://doi.org/10.2138/am-2022-8543. http://www.minsocam.org/

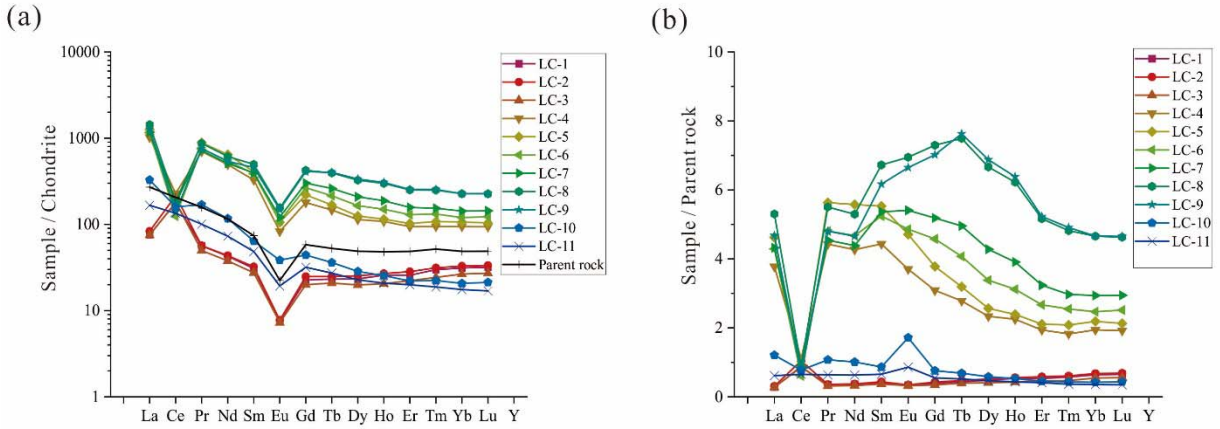

Figure 4. (a) Chondrite-normalized REE profiles for the different soil horizons and the parent rock. (b) Average REE concentration profiles for the different soil horizons normalized to the parent rock composition.

This is the peer-reviewed, final accepted version for American Mineralogist, published by the Mineralogical Society of America.
The published version is subject to change. Cite as Authors (Year) Title. American Mineralogist, in press.
DOI: https://doi.org/10.2138/am-2022-8543. http://www.minsocam.org/

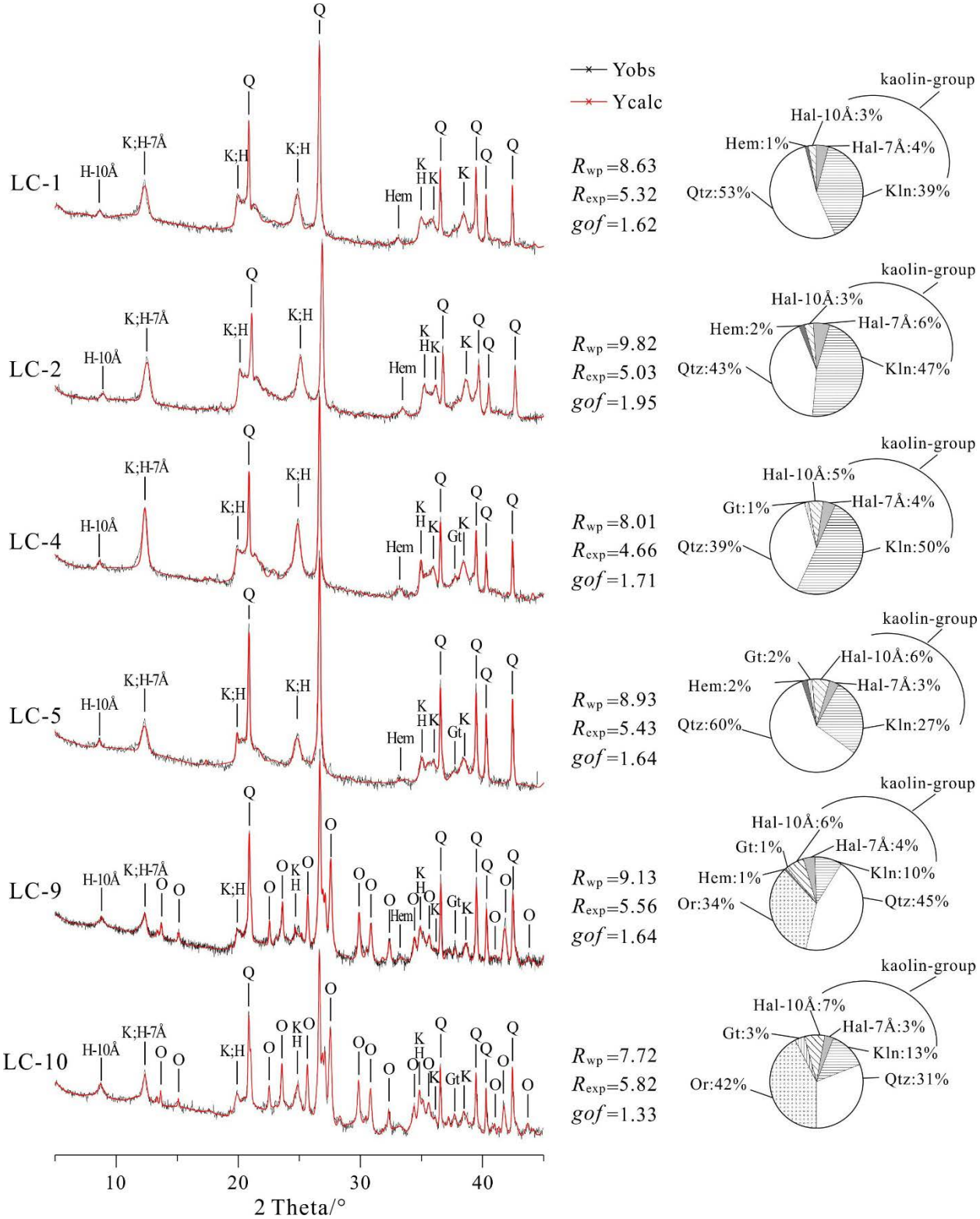

Figure 5. Representitive X-ray diffraction patterns and semi-quantitative analyses of the weathering profiles. K-Kal = kaolinite; H-Hal = halloysite; Q-Qzt = quartz; O-Or = orthoclase; G-Gt = goethite; He-Hem = hematite. Notes: kaolin-group minerals include: kaolinite, halloysite-7Å and halloysite-10 Å.

This is the peer-reviewed, final accepted version for American Mineralogist, published by the Mineralogical Society of America.
The published version is subject to change. Cite as Authors (Year) Title. American Mineralogist, in press.
DOI: https://doi.org/10.2138/am-2022-8543. http://www.minsocam.org/

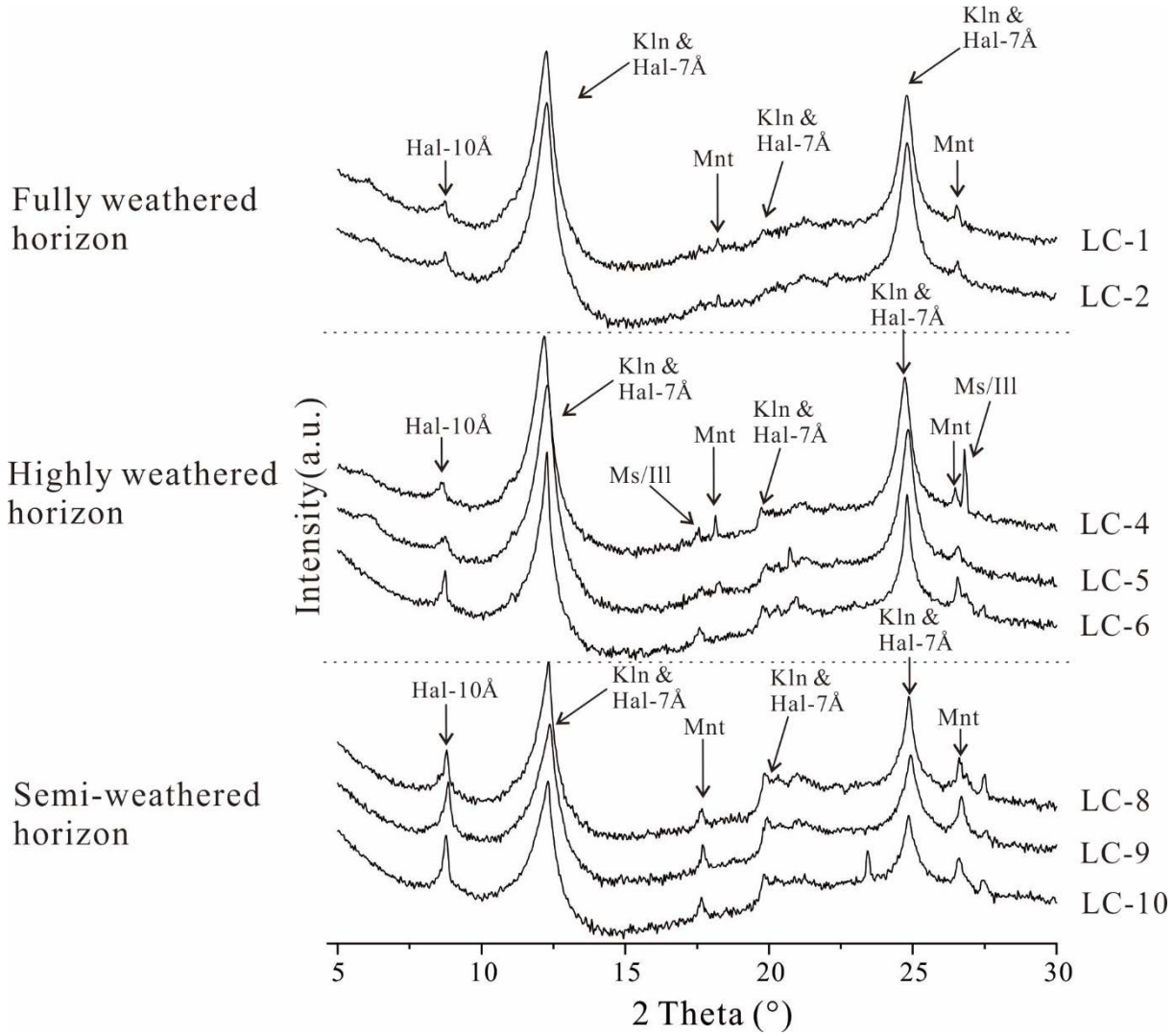

Figure 6. Representitive X-ray diffraction patterns of the clay fraction (< 2 μ m) from different regolith horizons. Kal = kaolinite; Hal = halloysite; Mnt = montmorillonite; Ms = muscovite; Ill = illite.

This is the peer-reviewed, final accepted version for American Mineralogist, published by the Mineralogical Society of America.
The published version is subject to change. Cite as Authors (Year) Title. American Mineralogist, in press.
DOI: https://doi.org/10.2138/am-2022-8543. http://www.minsocam.org/

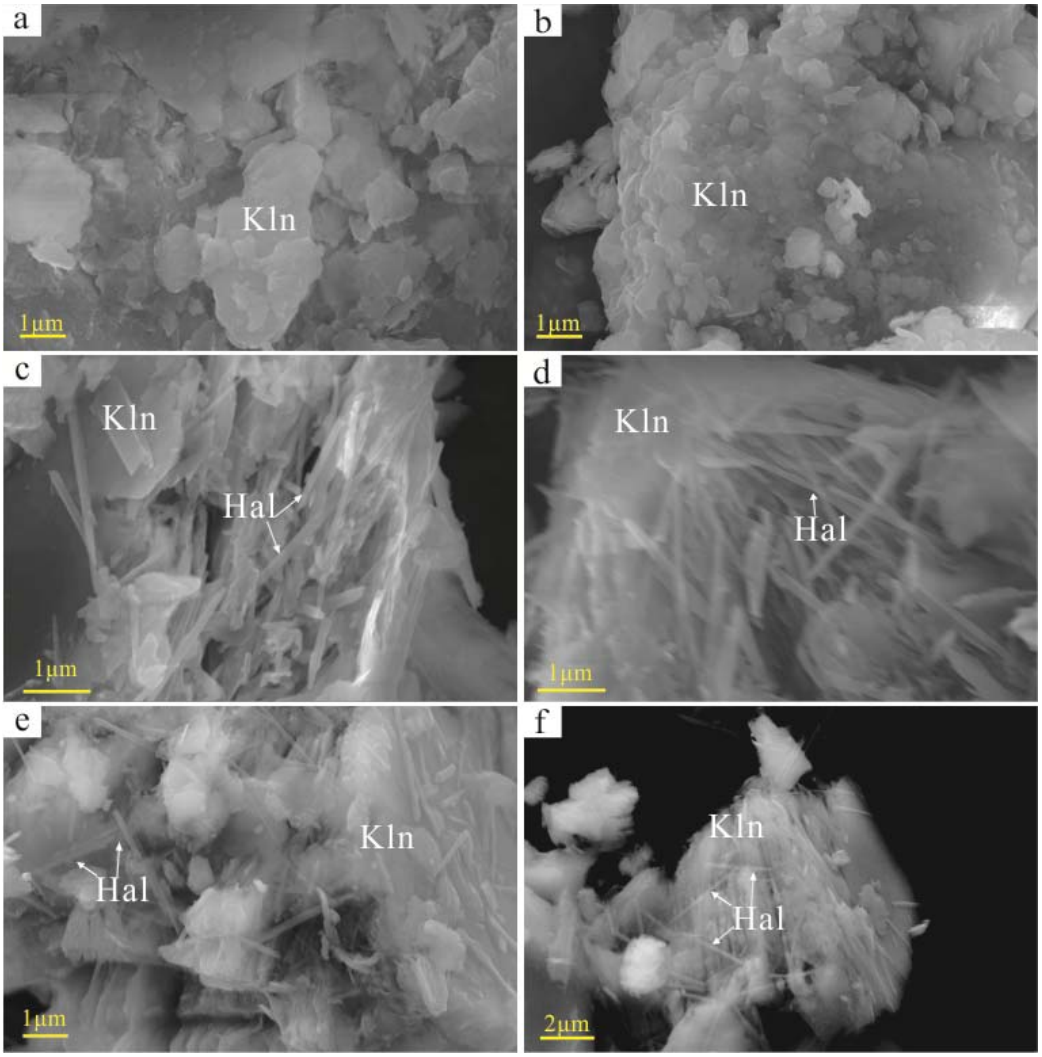

Figure 7. Scanning electron microscopy images of clay minerals in the weathering profiles. (a–b) Clay minerals in highly weathered horizons. (c–f) Clay minerals in semi-weathered horizons. Kln = kaolinite; Hal = halloysite.

This is the peer-reviewed, final accepted version for American Mineralogist, published by the Mineralogical Society of America.
The published version is subject to change. Cite as Authors (Year) Title. American Mineralogist, in press.
DOI: https://doi.org/10.2138/am-2022-8543. http://www.minsocam.org/

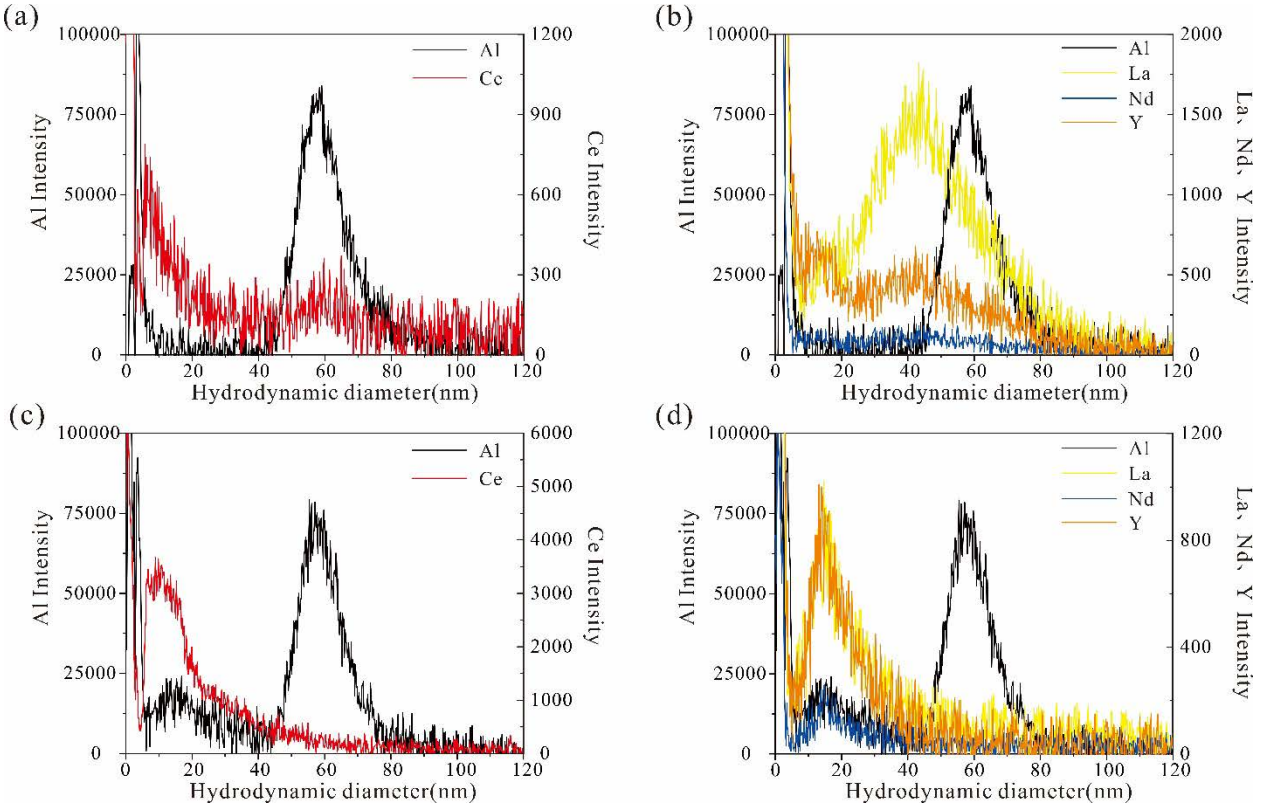

Figure 8. Size distribution of Al- and REE-bearing nano-particles measured by hollow fiber flow field-flow fractionation coupled with inductively coupled plasma-mass spectrometer from different weathering horizons. (a–b) highly weathered horizons and (c–d) semi-weathered horizons.

This is the peer-reviewed, final accepted version for American Mineralogist, published by the Mineralogical Society of America.
The published version is subject to change. Cite as Authors (Year) Title. American Mineralogist, in press.
DOI: https://doi.org/10.2138/am-2022-8543. http://www.minsocam.org/

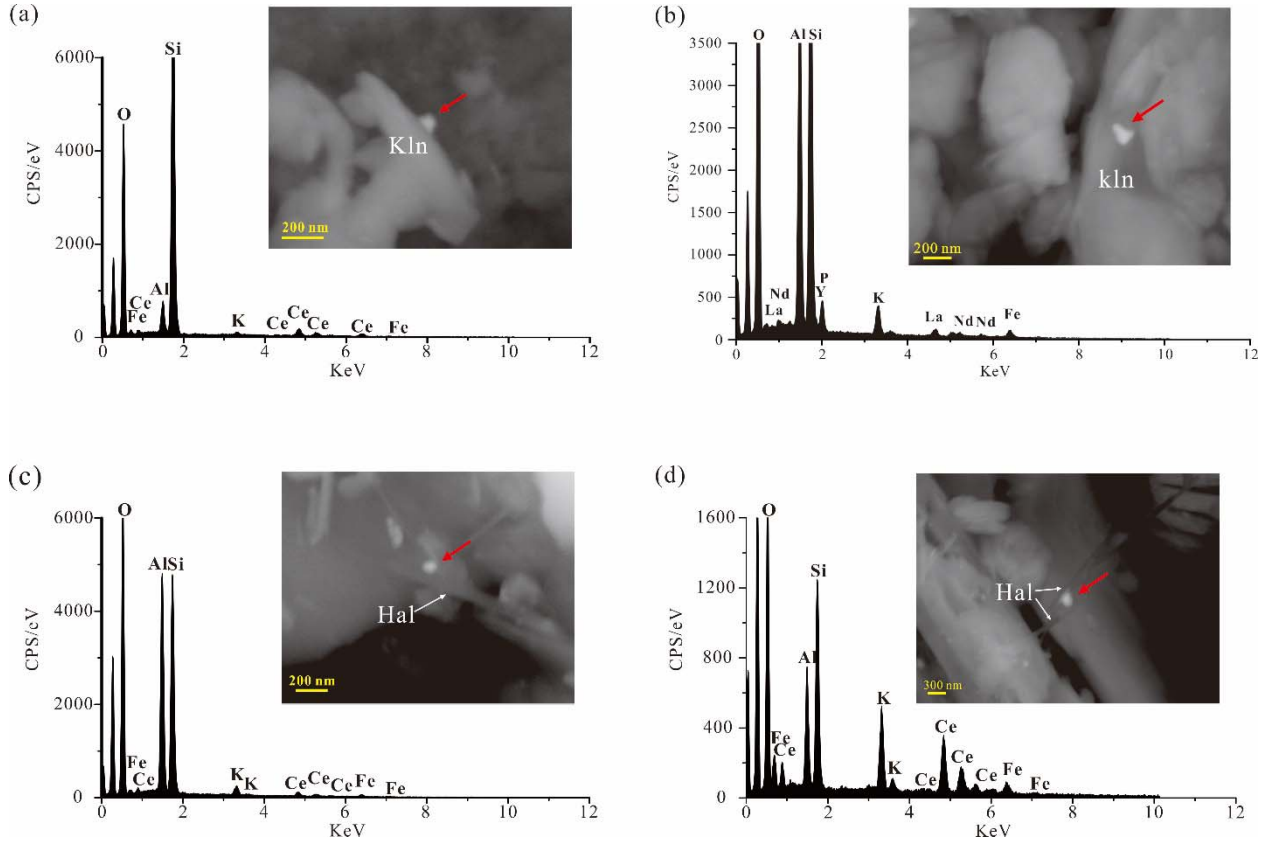

Figure 9. Scanning electron microscopy images of Ce nano-particles in (a–b) highly weathered horizons and (c–d) semi-weathered horizons. Arrows mark the Ce nano-particles. Kln = kaolinite; Hal = halloysite.

This is the peer-reviewed, final accepted version for American Mineralogist, published by the Mineralogical Society of America.
The published version is subject to change. Cite as Authors (Year) Title. American Mineralogist, in press.
DOI: https://doi.org/10.2138/am-2022-8543. http://www.minsocam.org/

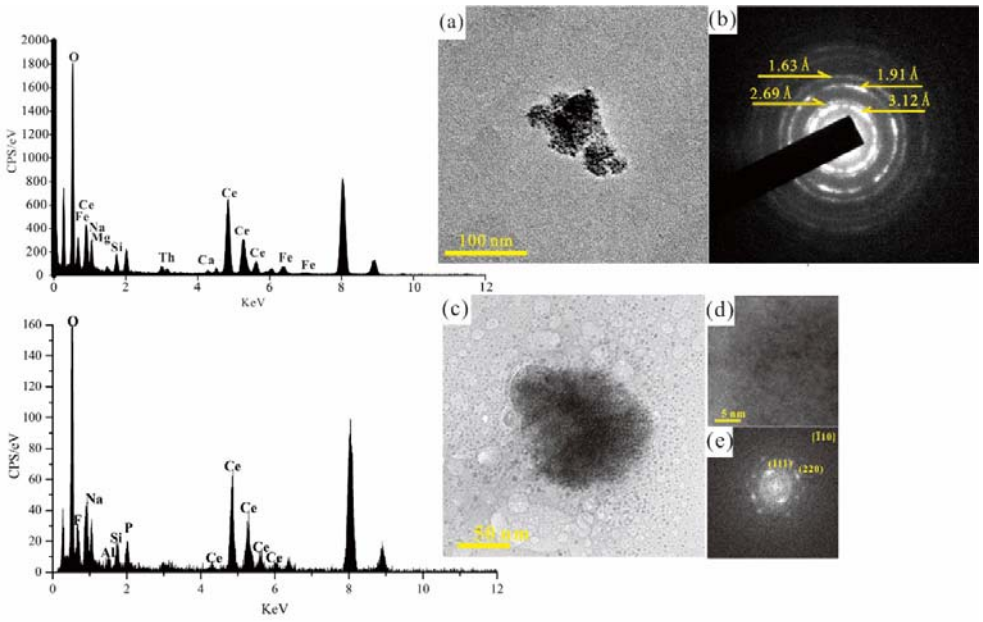

Figure 10. Transmitted electron microscopy images and diffraction patterns of (a) Ce-bearing particles (b) SEAD pattern showing the basis for the identification of the phase as cerite. (c) Ce-bearing particles (d) HRTEM image shows the nanocrystallites and (e) FFT image showing the basis for the identification of the phase as cerianite.

This is the peer-reviewed, final accepted version for American Mineralogist, published by the Mineralogical Society of America.
The published version is subject to change. Cite as Authors (Year) Title. American Mineralogist, in press.
DOI: https://doi.org/10.2138/am-2022-8543. http://www.minsocam.org/

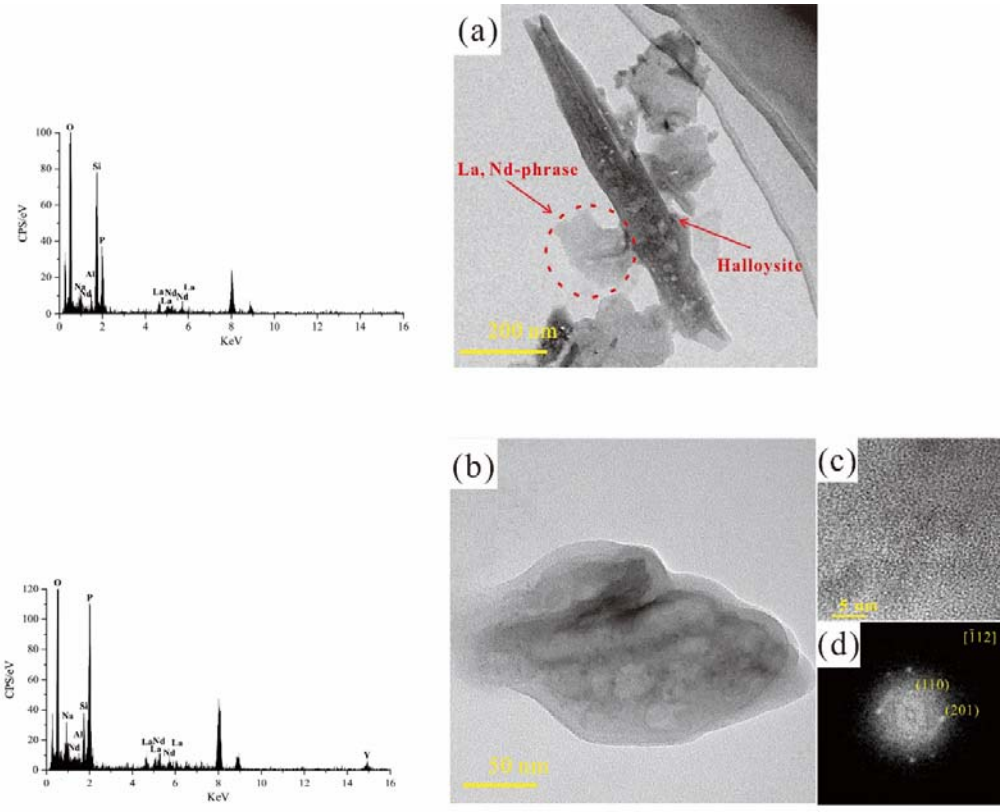

Figure 11. Transmitted electron microscopy images and diffraction patterns of (a) a La-Nd-bearing particle adhere onto the surface of a halloysite (b) La–Nd-Y-bearing nano-particle (c) HRTEM image shows the nanocrystallite and (d) FFT image showing the basis for the identification of the phase as rhabdophane-(La). Arrows mark the nano-particles.

945 ## Table Caption

946

947 **Table 1.** Operating parameters of the ultraviolet–visible spectrometer and inductively coupled
948 plasma–mass spectrometer.

UV−vis spectrometer	
Wavelength	254 nm for PS NPs
ICP-MS	
RF Power	1500 W
Nebulizer flow rate	0.40 mL/min
Plasma gas flow rate	15 L/min
Dwell time	500 ms
Isotopes monitored	^{27}Al, ^{89}Y, ^{139}La, ^{140}Ce, ^{141}Pr, ^{144}Nd, ^{147}Pm, ^{150}Sm, ^{152}Eu, ^{157}Gd, ^{159}Tb, ^{163}Dy, ^{165}Ho, ^{167}Er, ^{170}Tm, ^{173}Yb, ^{175}Lu

949

950